

ABSTRACT

Name: Timothy J. Maxwell

Department: Physics

Title: Diffraction Analysis of Coherent Transition Radiation Interferometry in
Electron Linear Accelerators

Major: Physics

Degree: Master of Science

Approved by:

Date:

Thesis Director

NORTHERN ILLINOIS UNIVERSITY

ABSTRACT

Electrons crossing the boundary from one medium to another generate bursts of transition radiation. In the case of compact electron bunches they will emit radiation more or less coherently and with an N_e -squared enhancement on wavelengths related to the longitudinal bunch distribution. This coherent transition radiation has therefore attracted much attention as an interceptive charged particle beam diagnostic technique. Many analytical descriptions have been devised for describing the spectral distribution generated by electron bunches colliding with thin metallic foils, often making different simplifying assumptions. With typical bunches having characteristic length scales in the submillimeter range, measurable spectra are generated up into the millimeter range. Detection and analysis of this radiation are then performed using optical equipment with dimensions of tens of millimeters. This gives rise to concern that optical diffraction effects may spread the wavefront of interest into regions larger than the optical elements and partially escape detection, generating a wavelength-dependent instrument response. Here I use a minimal C++ code implementing the methods of virtual photons and vector diffraction theory to analyze this effect in the Fermilab/NICADD photoinjector interferometer.

NORTHERN ILLINOIS UNIVERSITY

DIFFRACTION ANALYSIS OF COHERENT TRANSITION RADIATION
INTERFEROMETRY IN ELECTRON LINEAR ACCELERATORS

A THESIS SUBMITTED TO THE GRADUATE SCHOOL
IN PARTIAL FULFILLMENT OF THE REQUIREMENTS

FOR THE DEGREE
MASTER OF SCIENCE

DEPARTMENT OF PHYSICS

BY

TIMOTHY JOHN MAXWELL

© 2007 Timothy John Maxwell

DEKALB, ILLINOIS

DECEMBER 2007

Certification:

In accordance with departmental and Graduate School policies, this thesis is accepted in partial fulfillment of degree requirements.

Thesis Director

Date

ACKNOWLEDGEMENTS

I would like to thank all members of the NICADD accelerator group, most of all Philippe Piot, for their valuable input and guidance. Also, special thanks to my officemate James Younkin for enduring many thoughtful research discussions. Finally, my deepest gratitude to the late Courtlandt Bohn for being a tremendous role model and for introducing me to a field that never ceases to captivate my interest.

This study was supported by the U.S. Department of Energy under contract no. DE-FG02-06ER41435 with Northern Illinois University.

TABLE OF CONTENTS

	Page
LIST OF FIGURES	vi
Chapter	
1. INTRODUCTION	1
Transition Radiation	1
Coherent Transition Radiation	3
CTR Interferometry	7
Problem Statement	11
2. THEORY AND APPROACH	15
Ideal Optical Approximation	15
Method of Virtual Photons for Modeling Electrons	16
The Vector Diffraction Integral	20
3. NUMERICAL IMPLEMENTATION	25
THz Optical Transport Software	25
Basic Benchmarking	30
Limitations and Future Improvements	36
4. SINGLE-ELECTRON TRANSITION RADIATION MODELING	39
Transition Radiation Model Comparison	39
Transition Radiation Apex Trends	46

Chapter	Page
5. INTERFEROMETRY AND CTR MODELING	51
6. FINAL REMARKS	63
Conclusions	63
Future Plans	64
REFERENCES	67

LIST OF FIGURES

Figure	Page
1. Energy density distribution versus angle of observation computed from the Ginzburg-Frank equation for $\gamma = 50, 100$ and 200	2
2. Side view of interferometer elements showing acceptance and collimation of CTR.....	8
3. Top view of interferometer elements showing propagation of CTR wavefront after acceptance and collimation from foil.....	8
4. An example 3D mesh rendering.....	27
5. A flow chart showing the logical flow of the THOTS code.....	28
6. Far-field diffraction of a circular aperture.....	31
7. Extreme near-field diffraction of a circular aperture.....	32
8. Diffraction by 6" EFL, 2" O.D. 90° off-axis parabolic mirror in collimating mode.....	35
9. Spectral intensity distribution from backward single-electron radiation with circular foil at 45-degree incline.....	40
10. Spectral fluence traces along plane parallel to foil for far-field backward TR at normal incidence.....	42
11. Spectral fluence profiles along center plane for near-field backward TR at normal incidence	44
12. Spectral fluence traces along plane parallel to foil for near-field backward TR at normal incidence	45
13. TR apex location as a function of γ	48

Figure	Page
14. TR apex location as a function of r_{foil}	48
15. TR apex location as a function of λ	50
16. Schematic intensity profile of radiation propagating through an “unfolded” interferometer for single-electron TR.....	53
17. Intensity distribution images at instrument acceptance window and final detector for single-electron transition radiation for various λ	54
18. Response functions of acceptance aperture and instrument	57
19. CTR signal due to 300 μ m FWHM line charge distribution and subsequent correction using THOTS-calculated system frequency responses	61

CHAPTER I

INTRODUCTION

Transition Radiation

The background of my analysis begins with considering the problem of a single relativistic electron colliding at normal incidence with a thin, perfectly conducting foil of infinite extent. To solve Maxwell's equations for this basic system, one can use the method of images. We then construct a model system wherein the electron is approaching an oppositely charged image particle moving toward the electron with equal and opposite velocity in the lab frame. The result is a head-on collision in the plane originally containing the metallic foil.

Now let us analyze the moment the electron strikes the foil. This would be the same as the electron and our image "positron" colliding and annihilating in the model system. The energy would then be released in the form of what is referred to as the backward transition radiation (TR). This gives rise to the well-known Ginzburg-Frank formula for the spectral energy density (in SI units) [1]:

$$\frac{d^2U}{d\omega d\Omega} = \frac{e^2 \beta^2 \sin^2 \theta}{4\pi^3 \epsilon_0 c (1 - \beta \cos \theta)^2} \quad (1.1)$$

In this axially symmetric energy distribution per interval frequency, $\beta = v/c$, e is the electron charge and θ is the angle measured from the negative of the axis

defined by the electron's initial trajectory. This is valid for a relativistic electron colliding with an ideal conductor where the dielectric constant of the foil is real and satisfies $|\varepsilon| \rightarrow \infty$. A frequency-constant, metal-like response should be realistic at values well below the plasma frequency of the foil, as is our case ($\lambda > 0.1\text{mm}$). Also, this is only in the far-field when $R/\lambda > \gamma^2$, where R is the distance from the foil and γ the relativistic factor. The formula is plotted in Figure 1 for $\gamma = 50, 100$ and 200 .

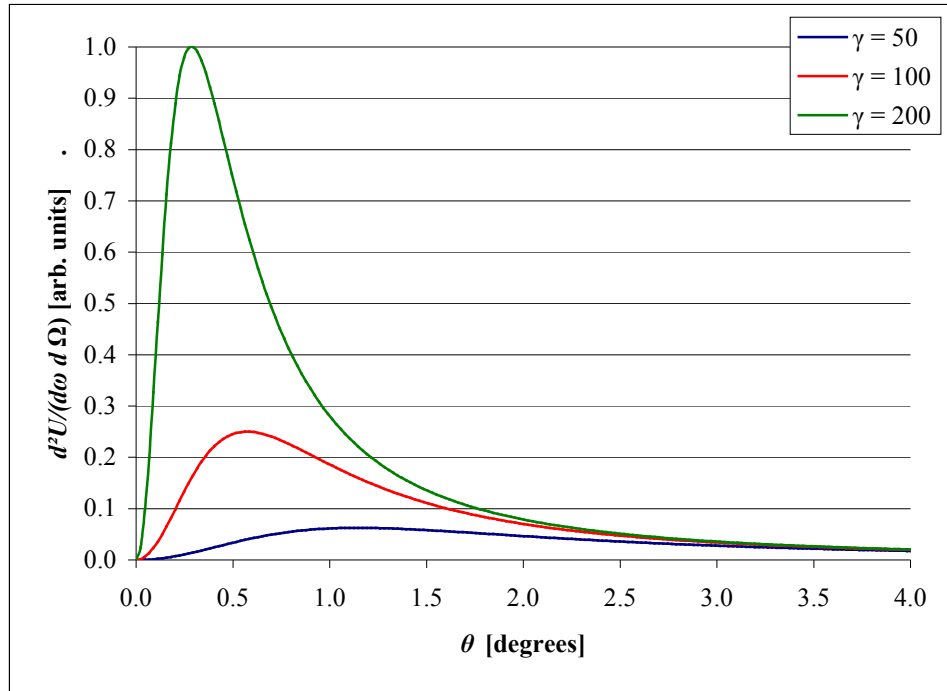


Figure 1. Energy density distribution versus angle of observation computed from the Ginzburg-Frank equation for $\gamma = 50, 100$ and 200 .

The derivation of this formula is straightforward and well studied in the literature and as such is not reproduced here. In [1, 2] the formula is also derived taking the dielectric properties of the foil into account. As we will continue to use the

perfect metal, “ideal mirror” approach later to account for other effects more relevant to this study, I will not explore these dielectric dependencies.

Noting again the rotational symmetry of the above energy distribution, we see that as the electron hits the foil the radiation produced is into the backward plane and focused along a tightly peaked cone. Also note the increase in overall intensity with larger γ . This is related to the increased energy released when instantaneously stopping the more energetic electron in our ideal theoretical system. Forward transition radiation is also observed. This is due to the reverse of the process above as the electron reforms and emerges on the other side of the foil.

We will see that this highly simplistic model carries the bulk of the general features of single-electron transition radiation. At the end of this chapter I will begin to address taking more of the relevant physics into account as they relate to this study.

Coherent Transition Radiation

For the moment let us continue to focus our attention on the phenomenon at hand and how it relates to the very practical and well-studied charged particle beam diagnostic technique to be introduced. In the case where several of these electrons collide with the foil as a bunch, one finds that the transition radiation will form approximately coherently. Furthermore, it does so in such a way as to make this radiation both measurable and quite practically useful.

The following approach is somewhat different than that typically found in the literature. Alternative derivations are readily available such as those in [3, 4, 5].

We continue here by analyzing the radiation associated with a single relativistic electron in frequency space. Representing the radiation field $\vec{E}(\omega, \vec{r})$ of the electron at a given frequency as the Fourier component of the field $\vec{E}_e(t, \vec{r})$ given off at some instant t times the complex phase factor:

$$\vec{E}_e(\omega, \vec{r}) = \vec{E}(\omega, \vec{r}) e^{i(\omega t - \vec{k} \cdot \vec{r})} \quad (1.2)$$

Here $\vec{k} = (\omega/c) \hat{n}$, where \hat{n} is the unit vector direction of the radiation's propagation.

Assuming a large number of densely packed, co-moving electrons to justify a continuum limit, for N electrons arranged in a normalized probability density $\rho(\vec{r})$, we get the total field of the bunch by superposition of the above field:

$$\begin{aligned} \vec{E}_{bunch}(\omega, \vec{r}) &= \int_{ALL\ SPACE} N \vec{E}_e(\omega, \vec{r} - \vec{r}') \rho(\vec{r}') d^3 r' \\ &= N \int_{ALL\ SPACE} \vec{E}(\omega, \vec{r} - \vec{r}') e^{i[\omega t - \vec{k} \cdot (\vec{r} - \vec{r}')] } \rho(\vec{r}') d^3 r' \end{aligned} \quad (1.3)$$

We then calculate the spectral energy density distribution of the resulting radiation:

$$\begin{aligned} I(\omega, \vec{r}) &\propto \vec{E}_{bunch}^* \cdot \vec{E}_{bunch} \\ &= N^2 \iint_{ALL\ SPACE} \vec{E}^*(\omega, \vec{r} - \vec{r}') \cdot \vec{E}(\omega, \vec{r} - \vec{r}'') e^{i[\vec{k} \cdot (\vec{r}'' - \vec{r}')] } \rho(\vec{r}') \rho(\vec{r}'') d^3 r' d^3 r'' \end{aligned} \quad (1.4)$$

Remembering we assume the system of electrons to be co-moving and additionally assuming that our observation point \vec{r} is far from the center of the bunch as compared to the extent of the bunch such that $\vec{r} \gg \vec{r}'$ and $\vec{r} \gg \vec{r}''$:

$$I(\omega, \vec{r}) \propto N^2 I_e(\omega) \iiint_{\substack{ALL \\ SPACE}} e^{i[\vec{k} \cdot (\vec{r}'' - \vec{r}')] } \rho(\vec{r}') \rho(\vec{r}'') d^3 r' d^3 r'' \quad (1.5)$$

where here $I_e(\omega)$ is the integrated value of $|\vec{E}(\omega, \vec{r})|^2$ over the source surface.

I pause here to point out an important feature of Equation (1.5). If we constrained our interest to wavelengths larger than the dimensions of our electron bunch, the phase factor present in the above integral would be quite small. Physically one might imagine the electrons of the bunch simultaneously emitting radiation with a separation of tens of micrometers. In the range of millimeters and up, the very small phase difference between our small radiators would be negligible and the interference would be largely constructive far from the bunch.

For typical bunch lengths in modern linear accelerators (hundreds of microns) this pseudo-coherence occurs in the THz regime. It is clear from the above expression that in this range the signal appears to be roughly that of a single electron's source field with a sizable N^2 enhancement over background. By colliding the bunch with a foil to generate the source electric field in Equation (1.5), we have what is referred to as the coherent transition radiation (CTR). Note that in such a case, if one uses the Ginzburg-Frank formula presented in Equation (1.1) to represent the modulus-squared term in Equation (1.5), all of the frequency dependence rides on the bunch distribution function since Equation (1.1) introduces no frequency dependence. This gives us a hint to explore the integral term above.

For a bunch with all particles traveling along the z -axis, i.e., as a line charge distribution, for perpendicular incidence on a thin foil we develop Equation (1.5):

$$I(\omega, \bar{r}) \propto N^2 I_e(\omega) \int_{-\infty}^{\infty} \int_{-\infty}^{\infty} e^{i[k(z''-z')] } \rho(z') \rho(z'') dz' dz'' \quad (1.6)$$

Here $\rho(z)$ is the longitudinal bunch distribution. Using $k \approx \omega / c$ and $z = c\beta t + z_0 \cong ct$, where we neglect the constant-phase initial position:

$$\begin{aligned} I(\omega, \bar{r}) &\propto N^2 I_e(\omega) \int_{-\infty}^{\infty} \int_{-\infty}^{\infty} e^{i[\omega(t''-t')]} \rho(t') \rho(t'') dt' dt'' \\ &= N^2 I_e(\omega) |f(\omega)|^2 \end{aligned} \quad (1.7)$$

Here we identify $f(\omega)$ as the complex Fourier transform of $\rho(t)$. The $f(\omega)$ term is frequently referred to as the “form factor” of the bunch.

Equation (1.7) shows more clearly the practical use of CTR. We now see that the coherent effect not only makes for an enhanced and measurable signal, but also that the frequency distribution of the detected transition radiation is directly related to the frequency distribution of the longitudinal bunch distribution. With an experiment designed to analyze the frequency spectrum of CTR emitted as a charged particle beam is shot through a foil, we can find the longitudinal distribution of the bunched beam, assuming the $|f(\omega)|^2$ term can be isolated. This is what is done in modern CTR experiments. However, removing all other frequency dependencies from Equation (1.7) can be difficult. A simplified model attempting this is analyzed in Chapter 5.

CTR Interferometry

With our goal now being to reconstruct the frequency spectrum of the CTR generated in our experiment, we turn to Michelson interferometry. In the following we will become more familiar with the instrument that is the subject of our interest, that is, the interferometer employed at the Fermilab/NICADD photoinjector laboratory. On the subsequent theory behind the instrument I borrow largely from a related analysis performed by group member Daniel Mihalcea [6].

Figures 2 and 3 show 3D renderings of the side and top views of the instrument, respectively. In the side view shown in Figure 2, we see the instrument from the perspective of the beam as it approaches the foil in the $+z$ -direction (into the page). The foil is pitched at a 45° angle. Though I have not yet discussed the effects of oblique incidence, this essentially directs the resulting backward CTR into an asymmetric cone at a 90° angle to the beam's trajectory.

Immediately after the foil there is a quartz viewing window. This serves as the separation between the interferometer and the vacuum necessary for the particle beam. With the CTR having some angular divergence dependent on the beam energy, the accepted radiation is then collimated using a 90° off-axis parabolic mirror. In our case, this has a 6" effective focal length (EFL). In the paraxial approximation, our once-divergent radiation is now propagating as a plane wave through the instrument. From there the wavefront is redirected by a gold mirror into the heart of the instrument, shown more clearly in the top view of Figure 3.

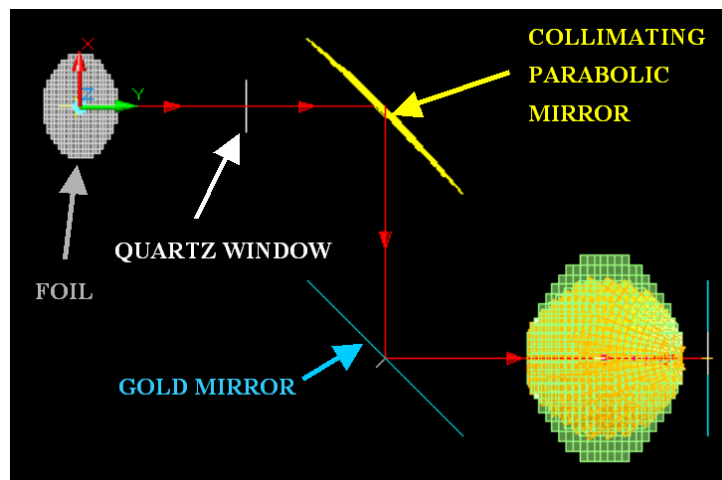


Figure 2. Side view of interferometer elements showing acceptance and collimation of CTR.

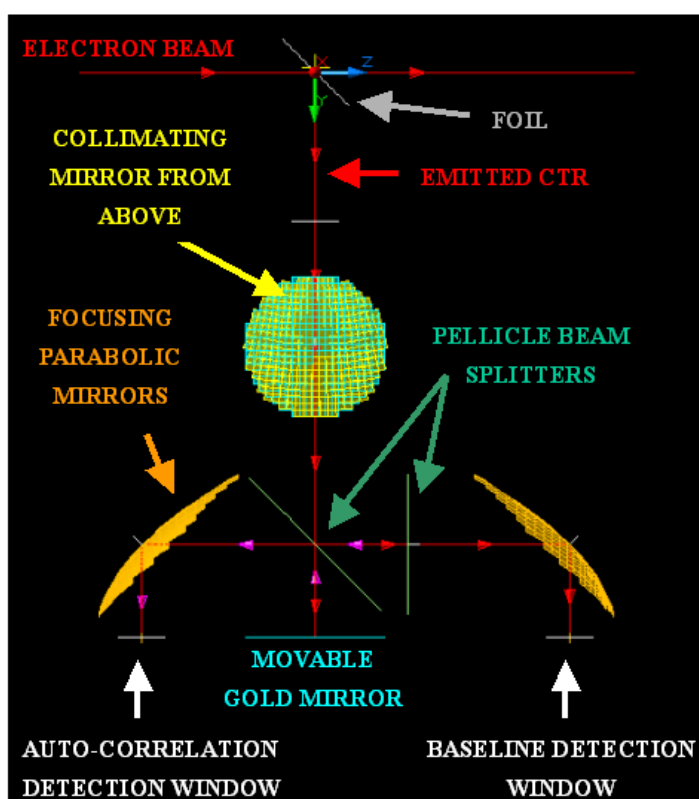


Figure 3. Top view of interferometer elements showing propagation of CTR wavefront after acceptance and collimation from foil.

In Figure 3, we see the layout for the Michelson interferometer portion of the instrument. The wavefront is split into two equal signals by the first beam splitter. The reflected portion then travels to a second beam splitter. The transmitted portion of this path is then focused by a 2" EFL parabolic mirror onto an observation window (shown on the right) where a detector is placed. This signal serves as a baseline to normalize the interference pattern measured at the window on the left to account for equipment jitter, etc.

Going back to the reflected portion at the second beam splitter, it is returned back through the first beam splitter and similarly imaged onto the observation window on the left after focusing. This will serve as the "fixed leg" of the interference pattern.

The "variable leg" of the interference pattern comes from the portion of the wavefront transmitted at first incidence with the first beam splitter. This is reflected off of a gold mirror placed on a precision motor-controlled movable stage. The return path then heads back to reflect off of the first beam splitter to be recombined with the fixed-leg wavefront and also imaged onto the observation window on the left.

In the event that both the movable mirror and the second beam splitter are exactly the same distance from the first beam splitter, we would of course expect maximum constructive interference. However, by changing the path length of the variable leg's movable mirror, we will see that one can find the autocorrelation function of the wavefront and thereby reconstruct the frequency spectrum of the emitted radiation.

For a plane wave with some transverse electric field distribution $E(t)$, the intensity I_1 measured at the “autocorrelation window” on the left is related to the sum of the fields of the fixed leg and path-delayed variable leg [6]:

$$I_1 \propto \int_{-\infty}^{\infty} |E(t) + E(t + \delta/c)|^2 dt \quad (1.8)$$

However, it is worth noting that due to jitter and other experimental imperfections, the wavefront may have some other imbedded noise. To account for this we use our baseline detector I_2 as a means to normalize the autocorrelation signal. We then define our autocorrelation function $S(\delta)$ in terms of these time (and frequency) integrated measurements [6]:

$$S(\delta) \equiv \frac{I_1}{I_2} \propto \frac{\text{Re} \left\{ \int E^*(t) E(t + \delta/c) dt \right\}}{\text{Re} \left\{ \int |E(t)|^2 dt \right\}} \quad (1.9)$$

In frequency space the path delay simply introduces a complex phase factor:

$$S(\delta) \propto \frac{\text{Re} \left\{ \int |E(\omega)|^2 e^{i\omega\delta/c} d\omega \right\}}{\text{Re} \left\{ \int |E(\omega)|^2 d\omega \right\}} \quad (1.10)$$

We determine this autocorrelation function experimentally by taking several measurements of the CTR pulse at the two detectors for a fixed path difference δ , then repeating the measurement for many values of δ . From Equation (1.10) we see that an inverse Fourier transform of $S(\delta)$ will recover the frequency distribution of the integrated intensity necessary for reconstruction of the bunch form factor presented in Equation (1.7) [6]:

$$I(\omega) \propto |E(\omega)|^2 \propto \int S(\delta) e^{-i\omega\delta/c} d\delta \quad (1.11)$$

Using this technique we can, in principle, recover the phase information of the integrated signal necessary to model the longitudinal bunch properties, as desired. I have made a great number of simplifying assumptions while laying out this basic introduction on the intent and method of CTR analysis. But with this primer in mind we are now prepared to discuss the corrections that are my intention to address here.

Problem Statement

With the information about the longitudinal bunch distribution being related to the frequency spectrum analyzed by the interferometer, we now ask what real-world limitations might suppress the measured frequency spectrum. The work alluded to earlier performed by Daniel Mihalcea [6] was regarding the effect of a less than perfect detector frequency response. In the case of the instrument being employed at the Fermilab/NICADD photoinjector, two different types of detectors are used. First is a pyroelectric detector, which is a solid-state device. Second was a Golay cell that operates on photo-acoustics and provides a much flatter frequency response. It is easy to imagine, however, that not accounting for instrument behavior could erroneously skew the results when trying to reconstruct the bunch profile. In the case of detector response this could alter the entire span of the spectrum.

With work on detector behavior having been studied [6], the question being explored in this thesis is regarding the frequency response of the interferometer itself.

Every optical element from the foil to the detection window can potentially alter our ideal, freely propagating CTR wavefront.

The overriding issue that we will discuss in this paper is diffraction effects. Consider that we're expecting to find the most useful information to be embedded in the tenths of millimeters to millimeter range owing to the size of our typical bunch. If this is the case, and we are using optical implements that have a typical aperture of tens to hundreds of millimeters, how much will diffraction effects alter the measurement? Could diffraction cause the wavefront to spread to a region greater than the extent of a subsequent optical element, effectively trimming the wavefront edge as a function of wavelength? Of course in an ideal world we would use optics that are as large as possible, but this quickly inflates instrument cost and size. So we will want to explore the overriding assumption that the wavefront does indeed remain well collimated traversing the instrument. We would suspect that the diffraction contribution to the wavefront's divergence will certainly only have an effect at increasing wavelengths or longer observation distances, as one might guess from general trends in very simple diffraction geometries.

For example, "infinite foils" are in somewhat limited supply realistically. Many analyses have been done, notably [3, 4], addressing the effects of using a finite circular foil. In the near field this tends to introduce a frequency dependence on the generation of CTR. Furthermore it is somewhat difficult to measure radiation being scattered back into the path of the beam, as is the case of normal incidence to the foil. As I noted earlier, this problem is easily avoided by pitching the foil with respect to

the beam. This not only redirects the backward CTR, but it also affects the shape of the wavefront [3, 4, 5]. Therefore, any diffraction technique used to analyze this problem should take these effects at the foil into account.

As the spacing of the optical elements is on the order of tens to hundreds of wavelengths, we also run into another challenge in calculating these patterns: a basic far-field calculation may not suffice. Some work has been done on using a paraxial approximation in conjunction with second-order phase factors to enhance the accuracy of the Fourier optics technique [4]. As shown in [4], this both enhances the analytical prowess of the Fourier optics method and also allows the incorporation of parabolic mirrors into the model. We also don't have to abandon the use of fast Fourier transforms (FFT) to keep calculations efficient.

However, the use of multiple optical elements is continually restricted by use of the paraxial approximation in the above method. This tends to squash trends of drifting divergence between elements that may be more prevalent in a fully three-dimensional solution. Also, the use of an FFT is prone to edge effects that are most easily solved by inclusions of large empty regions or denoising. This is a typical drawback to Fourier techniques, as our signal will always start off with finite spatial limitations and necessarily generate an infinite spatial frequency range. A technique that restricts our attention to regions of interest would be desirable. Furthermore, the second-order phase factors still incorporate some degree of approximation. Abandoning these approximations, if at all possible, would be ideal.

To meet all the above demands, this paper develops a technique to analyze as critically as possible how near-field diffraction limitations might affect CTR propagation in the Michelson interferometer at the Fermilab/NICADD photoinjector. The ultimate goal is to reproduce the effective frequency response of the instrument. All of this is done with the scales of diffraction dictated by the size of the instrument and the wavelengths of interest kept in mind. In doing so the simulation models the CTR from an arbitrary electron bunch configuration colliding with a metallic foil. The propagation of this radiation is then to be achieved using a fully 3D, near-field diffraction calculation. Furthermore, the propagation of the radiation from one region to the next is repeatable and energy conserving. This is to allow the modeling of several optical elements in series and also to ensure that our final comparisons of scale between different calculations are accurate.

CHAPTER II

THEORY AND APPROACH

Ideal Optical Approximation

As the problem at hand is largely one of handling freely propagating radiation, it seems natural to resort to the use of an optical physics approach. Throughout the remainder of this paper we will be working at any given time with a single frequency component of the radiation field for any given calculation. This method has some important advantages.

First of all, and most significantly, this makes available all the techniques of ordinary optics with regard to the free propagation of monochromatic radiation. That is, the problem reduces to solving the Helmholtz wave equation resulting from a solution of Maxwell's equations *in vacuo* at a single frequency. An attempt to solve for the full three-dimensional boundary value problem in the time domain directly proves challenging.

We also have the advantage of easily calculating frequency spectra, which is ultimately something of great interest as a matter of comparison to both the theory and experiment outlined in the first chapter. There is also a disadvantage to this as it will then be necessary to perform repeated calculations for all frequencies of interest to generate a reasonably complete spectrum.

Finally, manipulations of the traveling field, especially frequency-dependent effects, are easily achieved at any time. This can prove useful, for instance, in the analysis of dispersive effects in the quartz window separating the instrument from the beam line.

While being able to account for the real and complex frequency dependencies of optical elements, the scope of this investigation is limited to ideal materials. I assume all reflecting surfaces to be those of perfectly conducting metallic mirrors. Any transmitting elements are also assumed to be perfectly transmitting.

Whatever the method of solving the vector wave equation, it is clear that some technique is needed for working with the field of the bunch in frequency space. Without this we have no way to model our source CTR field to begin with. To do this we turn to the method of virtual photons.

Method of Virtual Photons for Modeling Electrons

To bring the radiation field associated with an electron into a frequency space representation amenable to the modeling of CTR, I employ the method of virtual photons [4, 7]. Simply put, we represent an electron as the field of photons associated with its electromagnetic field. This holds very well for highly relativistic electrons whose fields are similar to a photon plane wave. For typical electron beams with energies in the MeV range this demand is easily met.

In order to get the frequency spectrum of the virtual photon field we perform the time Fourier transform of the relativistic electron's field. In the time domain the

field is easily derived by a Lorentz boost of the stationary electron field. The components in SI units and cylindrical coordinates for a charge q moving along the $+z$ -axis is:

$$\begin{aligned} E_r(r, z, t) &= \frac{\gamma q}{4\pi\epsilon_0} \frac{r}{\left[r^2 + \gamma^2(z - c\beta t)^2\right]^{3/2}} \\ E_z(r, z, t) &= \frac{\gamma q}{4\pi\epsilon_0} \frac{z - c\beta t}{\left[r^2 + \gamma^2(z - c\beta t)^2\right]^{3/2}} \end{aligned} \quad (2.1)$$

I use the symmetrically normalized Fourier integrals:

$$\begin{aligned} E(r, z, t) &= \frac{1}{\sqrt{2\pi}} \int_{-\infty}^{\infty} \tilde{E}(r, z, \omega) e^{i\omega t} d\omega \\ \tilde{E}(r, z, \omega) &= \frac{1}{\sqrt{2\pi}} \int_{-\infty}^{\infty} E(r, z, t) e^{-i\omega t} dt \end{aligned} \quad (2.2)$$

As we proceed with the transformation, we must be careful in accounting for the z -dependence as $z = z(t)$:

$$\begin{aligned} \tilde{E}_r(r, z_0, \omega) &= \frac{\gamma q}{2(2\pi)^{3/2} \epsilon_0} \int_{-\infty}^{\infty} \frac{r e^{-i\omega t}}{\left[r^2 + \gamma^2(z_0 - vt)^2\right]^{3/2}} dt \\ \tilde{E}_z(r, z_0, \omega) &= \frac{\gamma q}{2(2\pi)^{3/2} \epsilon_0} \int_{-\infty}^{\infty} \frac{(z_0 - vt) e^{-i\omega t}}{\left[r^2 + \gamma^2(z_0 - vt)^2\right]^{3/2}} dt \end{aligned} \quad (2.3)$$

where now z_0 denotes the z position of the electron at “the moment of the transformation.” To take care of the composite nature of the integral, we make the substitution $t' = t + z_0/v$. The substitution is valid for an electron moving with constant velocity. It is a statement that the field of an electron at position z_0 is equivalent to that of one at the origin advanced appropriately forward in time:

$$\begin{cases}
\tilde{E}_r(r, z_0, \omega) = \frac{\gamma q}{2(2\pi)^{3/2} \epsilon_0} \int_{-\infty}^{\infty} \frac{r e^{-i\omega(t'-z_0/v)}}{[r^2 + (\gamma v t')^2]^{3/2}} dt' \\
\tilde{E}_z(r, z_0, \omega) = \frac{-\gamma q}{2(2\pi)^{3/2} \epsilon_0} \int_{-\infty}^{\infty} \frac{v t e^{-i\omega(t'-z_0/v)}}{[r^2 + (\gamma v t')^2]^{3/2}} dt'
\end{cases}$$

$$\begin{cases}
\tilde{E}_r(r, z_0, \omega) = \frac{\gamma q e^{i\omega z_0/v}}{2(2\pi)^{3/2} \epsilon_0} \int_{-\infty}^{\infty} \frac{r e^{-i\omega t'}}{[r^2 + (\gamma v t')^2]^{3/2}} dt' \\
\tilde{E}_z(r, z_0, \omega) = \frac{-\gamma q v e^{i\omega z_0/v}}{2(2\pi)^{3/2} \epsilon_0} \int_{-\infty}^{\infty} \frac{t' e^{-i\omega t'}}{[r^2 + (\gamma v t')^2]^{3/2}} dt'
\end{cases}$$

$$\begin{cases}
\tilde{E}_r(r, z_0, \omega) = \frac{q\omega}{(2\pi)^{3/2} \epsilon_0 \beta^2 c^2 \gamma} K_1\left(\frac{\omega}{\beta c \gamma} r\right) \exp\left(\frac{i\omega}{\beta c} z_0\right) \\
\tilde{E}_z(r, z_0, \omega) = \frac{-iq\omega}{(2\pi)^{3/2} \epsilon_0 \beta^2 c^2 \gamma^2} K_0\left(\frac{\omega}{\beta c \gamma} r\right) \exp\left(\frac{i\omega}{\beta c} z_0\right)
\end{cases} \quad (2.4)$$

Here K_0 and K_1 refer to the modified Bessel functions of the second kind of orders zero and one, respectively. In the last step the final integrations were performed using *Mathematica* [8] and are in agreement with [4]. I have also substituted the velocity with the relativistic equivalent $v = \beta c$. Note that the z component of the field is a factor of $(1/\gamma)$ smaller than the radial field. It is retained in our calculations, though it is typically neglected for highly relativistic beam simulations.

Finally, we will need the magnetic field information as well. This can be easily found using the relation $\vec{B} = (\vec{\beta} \times \vec{E})/c$ with the solution of Equation (2.4). The only surviving component is:

$$\tilde{B}_\phi(r, z_0, \omega) = \frac{q\omega}{(2\pi)^{3/2} \epsilon_0 \beta c^3 \gamma} K_1\left(\frac{\omega}{\beta c \gamma} r\right) \exp\left(\frac{i\omega}{\beta c} z_0\right) \quad (2.5)$$

An alternative derivation by direct solution of Maxwell's equations is also presented in [4].

Thus we have the photon field associated with a relativistic electron. The utility of this in the simulation of CTR is realized when we consider an idealized characterization of what occurs at a metallic foil. Looking back to our original ideal model, we can on one hand consider a collision with the foil to completely annihilate. In this description the self-field of the electron is released and radiated away from the surface of the foil.

From an alternative optical standpoint we can view the foil as a perfect mirror on one side and a finite aperture on the other. As the field of the electron approaches the foil, its virtual photon field is reflected, producing backward transition radiation. On the other side the foil behaves as a finite aperture in an opaque screen that is being illuminated by the electron, thus generating the forward transition radiation.

So to generate our initial TR optical front we compute the field across the surface of the foil at a given frequency. This then acts as our optical source being released as monochromatic radiation propagating through the instrument. To include CTR effects in the presence of many electrons, we simply add their fields by

superposition in configuration space. With a method for modeling the CTR we are left to find a satisfactory diffraction solution to describe the propagation of the electromagnetic wave.

The Vector Diffraction Integral

I should begin this section with a justification of applying a complete vector diffraction integral, as such an approach can be very cumbersome. The overriding goal in the development of this thesis is to discard as many of the approximations as possible in applying a rigorous optical approach.

The *ansatz* is that we start out knowing the only radiation source in an otherwise field-free region of space is from a finite aperture illuminated by some incident wave. We then wish to know what the intensity distribution is at some point in space beyond the aperture due to the spreading out of the wavefront. I therefore carry forward the optical treatment by recognizing this as the problem of diffraction when treated monochromatically.

We might first consider the application of a scalar Huygen's principle [9]. All the source photons are simply treated as spherically radiating electric field wavefronts. The contributions from each of these wavefronts are subsequently summed at the point of observation. We can however discard this immediately as the method breaks down quickly in the near field. This is owing, in part, to no preference being given to the source photon's trajectory.

We might consider the scalar Kirchoff formulation of diffraction optics [9] to correct for this effect. This is a step in the right direction as it begins to give some preference to the propagation direction by the introduction of an inclination factor. However this method still loses some very important information along the way. The result of these calculations is the magnitude of the transverse electric field. While we may be able to calculate near-field intensity patterns, we have lost all information regarding the new direction of propagation. We then lose the ability to use this solution as a field source for a subsequent diffraction calculation. This is a problem if we wish to image from one optical element to the next several times, as is the case in this investigation.

I pause here to note that for quick calculations other assumptions may be introduced to try and salvage the scalar Huygen, Kirchoff or Fresnel methods. By making careful paraxial assumptions and/or introducing second-order phase factors [4], one can still produce reasonably accurate results. However, I find it hard to fully justify the use of paraxial approximations when off-axis parabolic mirrors are to be analyzed. This is especially true if radiation is incident near the edges of concave mirrors. Large variations in deflection angle can manifest themselves, potentially rendering the paraxial approximation invalid.

Accounting for these concave mirrors can be a very challenging task when trying to solve for the intensity distribution analytically. Early in the pursuit of this research some attempts were made at ray tracing methods to avoid intermediate

calculations at the mirrors. This involves the solution of the parabolic equations that invariably lead to approximations for a closed-form solution.

But note that none of this would be necessary if the full vector electromagnetic field information were available during a calculation. The surface normal across the entire mirror's surface is well defined. We could in theory calculate the field at the mirror surface due to illumination by a distant aperture. After this the polarization and surface normal dependent reflection conditions at a metallic surface can be applied. The result is then used as our new source for subsequent diffraction calculations. All of the necessary physics are then preserved without (significant) approximation.

Therefore, in order to maintain valid near-field solutions and the vectorial information necessary for subsequent diffraction calculations and 3D reflections, we turn to application of a full vector diffraction solution.

The study of vector diffraction is well documented starting around 1940. At this point there was considerable interest in how buildings interfered with microwaves and radio waves. A good introduction to the problem is available in Jackson [10]. A look at this and other elaborate solutions [11, 12] yield many rather ugly-looking diffraction integrals. It quickly becomes clear that a diffraction solution that will obey Maxwell's equations will involve the need for a numerical solution.

One diffraction integral solution that accommodates a generalized computational approach quite nicely was found [13]. In this paper a very careful and elegant treatment of the effect on incident radiation of a partially exposing opaque screen is performed. As part of the construction, a symmetrized set of Maxwell's

equations is used, introducing the magnetic charge. This is done in much the same way one would construct magnetic charge or a magnetic scalar potential in the solution of basic electrodynamics problems [10]. In [13], surface electric and magnetic currents in an opaque screen that precisely neutralize the blocked parts of the wavefront are calculated to make the screen truly “opaque” in regions where there is no opening. This leaves only the partially exposed wavefront. In this construction the remaining points on the wavefront are then treated as secondary vector wave sources of orthogonal oscillating electric and magnetic dipoles as a vector Huygen principle. The result gives the electric and magnetic fields anywhere in the space beyond the screen in terms of an integration of the fields over the aperture in the screen [13]:

$$\left\{ \begin{array}{l} \bar{E}(\bar{r}) = \frac{-i}{2\lambda^2} \iint_{Aperture} \left\{ [1 + \hat{R} \cdot \hat{n}] \bar{E}(\bar{r}') - [\hat{R} \cdot \bar{E}(\bar{r}')] [\hat{R} + \hat{n}] \right\} [\exp(ikR)/R] d^2 r' \\ \quad + \frac{1}{2\lambda^2} \iint_{Aperture} \left[(\hat{R} \cdot \hat{n}) \bar{E}(\bar{r}') - (\hat{R} \cdot \bar{E}(\bar{r}')) \hat{n} \right] [\exp(ikR)/kR^2] d^2 r' \\ \bar{B}(\bar{r}) = \frac{-i}{2\lambda^2} \iint_{Aperture} \left\{ [1 + \hat{R} \cdot \hat{n}] \bar{B}(\bar{r}') - [\hat{R} \cdot \bar{B}(\bar{r}')] [\hat{R} + \hat{n}] \right\} [\exp(ikR)/R] d^2 r' \\ \quad + \frac{1}{2\lambda^2} \iint_{Aperture} \left[(\hat{R} \cdot \hat{n}) \bar{B}(\bar{r}') - (\hat{R} \cdot \bar{B}(\bar{r}')) \hat{n} \right] [\exp(ikR)/kR^2] d^2 r' \end{array} \right. \quad (2.6)$$

Here \bar{r} is the observation point, \bar{r}' is a vector to a point on the surface of the aperture, \bar{R} is the relative vector $\bar{R} = \bar{r} - \bar{r}'$, and \hat{n} is the unit Poynting vector of the field at the source (the propagation direction of the source radiation). I have also added the second integral terms in $1/kR^2$ that are left out as an approximation in [13]. The fields presented are the complex single-frequency components of a complete field solution.

In Equation (2.6) we find a vector Huygen principle that produces a solution to the Helmholtz equation. Furthermore, the solution is given solely in terms of an integral of the electromagnetic field over the surface it is emerging from. By evaluating both the electric and magnetic components and performing a simple cross product, we can also reproduce the Poynting vector field. This is useful both for repeated applications of the above diffraction integral as well as for calculation of time-averaged intensity distributions.

Even this integral seems complex and certainly would pose an analytical challenge if applied to fully general radiation sources and 3D geometries. It is interesting to note that by studying a single point source using this integral, one reproduces the Kirchoff inclination factor in a vector form [13]. This resemblance may have the reader questioning if Equation (2.6) is overly complicated. But despite its appearance, it is in fact an excellent candidate for a very simple and fully general numerical approach.

CHAPTER III

NUMERICAL IMPLEMENTATION

THz Optical Transport Software

With the intense analytical complexity of the solution developed in the previous chapter, we turn to a numerical approach. This has some serious drawbacks. Not the least of these is computational expense. The direct integration of Equation (2.6) will scale the computing time as N^2 . The higher the resolution we demand of our results, the longer the processing time. But I have found that low-resolution test runs can be performed during a simulation setup that takes just a couple of minutes on a typical personal computer before committing to a full analysis.

The other primary drawback is the analysis of general trends or computation of frequency spectra. Unlike a single-shot analytical solution, we are forced to select our points of interest and run calculations for several values of, for instance, ω . For this reason I have incorporated all of the above formulae into a minimal C++ code.

The primary motivation is to keep the scope of the calculations and libraries as focused as possible to minimize computation time. Second, with access to the NICADD computer cluster at Northern Illinois University we have the good fortune of being able to perform network-deployed simulations. This is easily achieved for compiled C++ code. At present this advantage is used when the same simulation must

be run for varying values of a given parameter. Each node on the cluster is assigned a different value of that parameter. In this way as many as ~50 different values can be evaluated simultaneously, reducing the turnaround time for high-resolution results.

The resulting code has been titled THz Optical Transport Software (THOTS). The purpose of the code is to use Equation (2.6) to propagate the image of a finite-source electromagnetic wave to another region in space. This is accomplished by way of a mesh technique to simplifying code writing. Two associated classes are generated for the mapping of the fields.

The first definition is a surface class. Surfaces are broken up into a discrete mesh. Figure 4 shows a 3D rendering of a very crude, low-resolution mesh of the 2” effective focal length focusing parabolic mirror of the Fermilab/NICADD photoinjector interferometer. The view is looking into the concave reflecting surface. The surface class provides storage for the geometrical information of each individual element of the mesh. The data included are the position of the center of the mesh element, the unit normal at the center, and two vectors which define the size and orientation of the element’s edges.

From a programming perspective the purpose of the surface class is to provide a map from some indices i and j to geometrical values across the 3D region. This makes the writing of looping functions much easier. Furthermore, this process reduces redundant calculation of the surface geometry. After a surface is defined, a function is called which assigns the appropriate values to all the elements of the class. The functions that fill the surface class with geometrical data are all written in terms of

general parameters. For instance, the parabolic mirror of Figure 4 can easily be regenerated with different orientations, dimensions, or focal lengths.

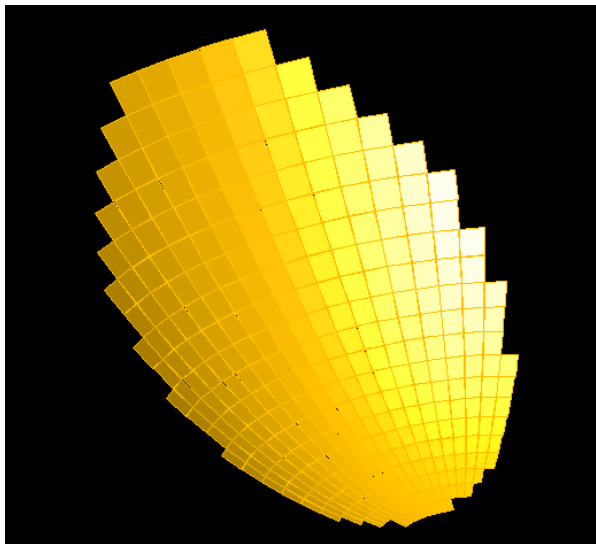


Figure 4. An example 3D mesh rendering. The 2" EFL parabolic mirror used for focusing in the subject interferometer as generated by the THOTS code shown here.

With all of the relevant information present in the surface class, a convenient class function was added. This function outputs an AutoCAD® script that, when opened, generates a 3D model of the mesh. All schematic 3D renderings for this thesis, such as those in Figures 2, 3, and 4, were rendered using this feature. We see that verifying the relative positions and orientations of the different surfaces being modeled becomes a simple matter. If interested, the user also has the option to inspect the spacing and sizes of the individual mesh elements or check for gaps in the mesh.

Associated with the surface is an EM grid. The EM class is similar to the surface class in that it maps field information to discrete indices. It provides storage

for the complex electric field vector, magnetic field vector, the real magnitude of the Poynting vector, and the direction of the Poynting vector. This in conjunction with a surface object defines the values of a discrete electromagnetic field in space.

A flow chart showing the process used by the code is illustrated in Figure 5.

The general approach starts with defining the first aperture then filling it with a source field. To model canonical diffraction patterns, this is an aperture filled with a monochromatic plane wave. In the case of CTR due to a bunch we evaluate the field due to several superpositions of Equations (2.4) and (2.5). The values across the foil's surface are then reflected by the usual conditions at a metallic surface [10].

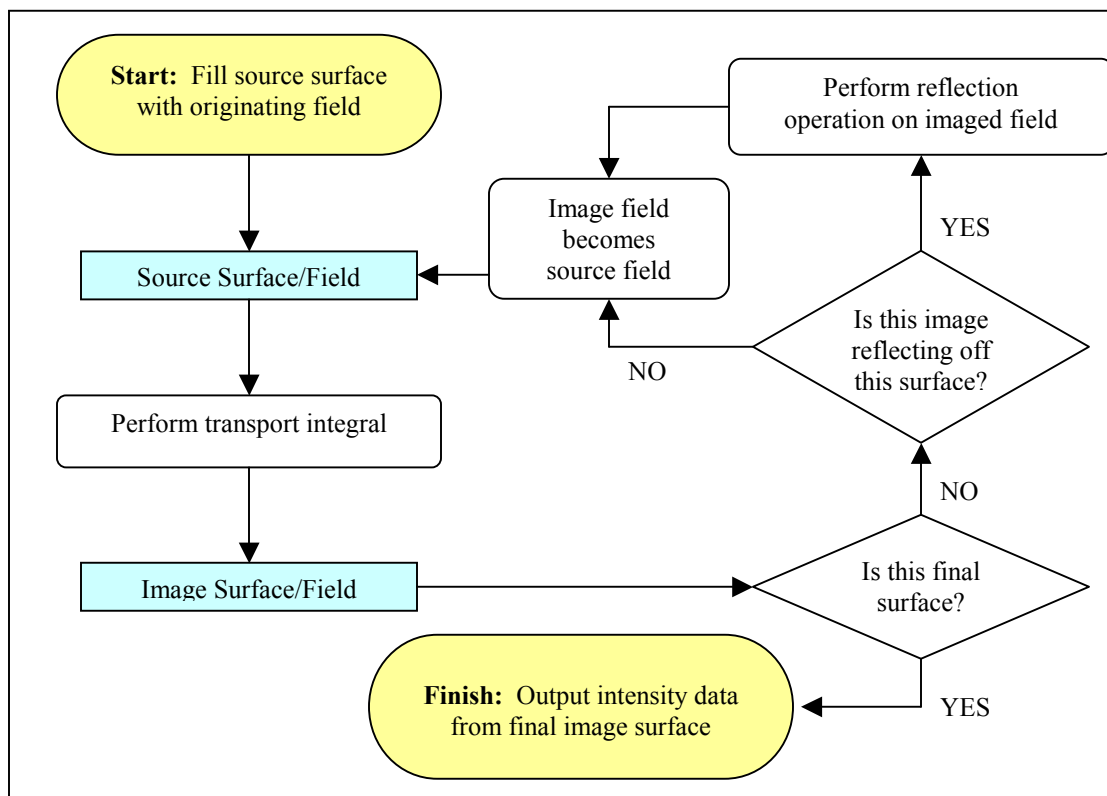


Figure 5. A flow chart showing the logical flow of the THOTS code.

After our source field is generated, the EM grid associated with a second surface is filled using the “transport integrals” in Equation (2.6). This requires evaluation of the integrals at every point along the second mesh.

If this second surface is a secondary aperture, such as the quartz window of the interferometer in Figures 2 and 3, then we repeat the transport integral of Equation (2.6) to find the field on a third surface. If this second surface were a mirror we would do the same thing, but first perform a reflection operation to the image field.

Eventually we will reach the end of our optical system. Here we would place a “virtual detection plane.” Once the field reaches this plane we perform the dot product of the Poynting vector with the surface normal to evaluate the intensity that would be measured on this surface. This serves as the final output of the THOTS code and displays the intensity distribution measured at our final virtual detection plane.

At this time THOTS implements a basic Euler method for evaluating Equation (2.6) as well as for the integrated spectral energies. Other integration methods were difficult to implement, as they require calculation of additional data points for curve fitting. Failure to include these points enhances the “numerical diffraction grating” effect. For evaluation of the modified Bessel functions for the electron field equations I followed the prescription given in *Numerical Recipes in C* [14]. Both the integrator and K_α libraries introduce error that is difficult to quantify in this complex calculation. For the following analyses, convergence was still found within acceptable run times. Comments on the present state of THOTS performance, the numerical grating effect, as well as some suggestions for future improvements follow at the end of this chapter.

Basic Benchmarking

To verify THOTS accuracy, several well-studied patterns were analyzed. Using plane polarized light sources, square apertures, square apertures at oblique incidence, and circular apertures the diffraction patterns in the near and far field were investigated. Here I present some results for a circular aperture as all of the optical elements in the interferometer have some circular section. The motivation is that this investigation might lend some insight into how the circular masking of the optics modulates the CTR signal.

First we analyze the far field for a circular aperture. Shown in Figure 6 is the irradiance profile through the center plane extending away from a circular aperture of radius 12.7 mm (1" O.D.) being illuminated by 1mm wavelength light. Inset in Figure 6 is a plot comparing a trace at a distance of 1.6 meters with the far-field Huygen's principle approximation [9]. We see in the far field that the THOTS code is in excellent agreement with expectation.

Second is a test in the extreme near field, shown in Figure 7. Here the same 1" O.D. aperture is again illuminated by a 1 mm wavelength plane wave. All along the wavefront we find typical examples as calculated using the near-field scalar Fresnel technique [9]. Inset in Figure 7 there is again an example trace, this time at a distance of 45 mm. Below this is a pattern calculated by a computational Fresnel method available through the University of Arizona College of Optical Science [15].

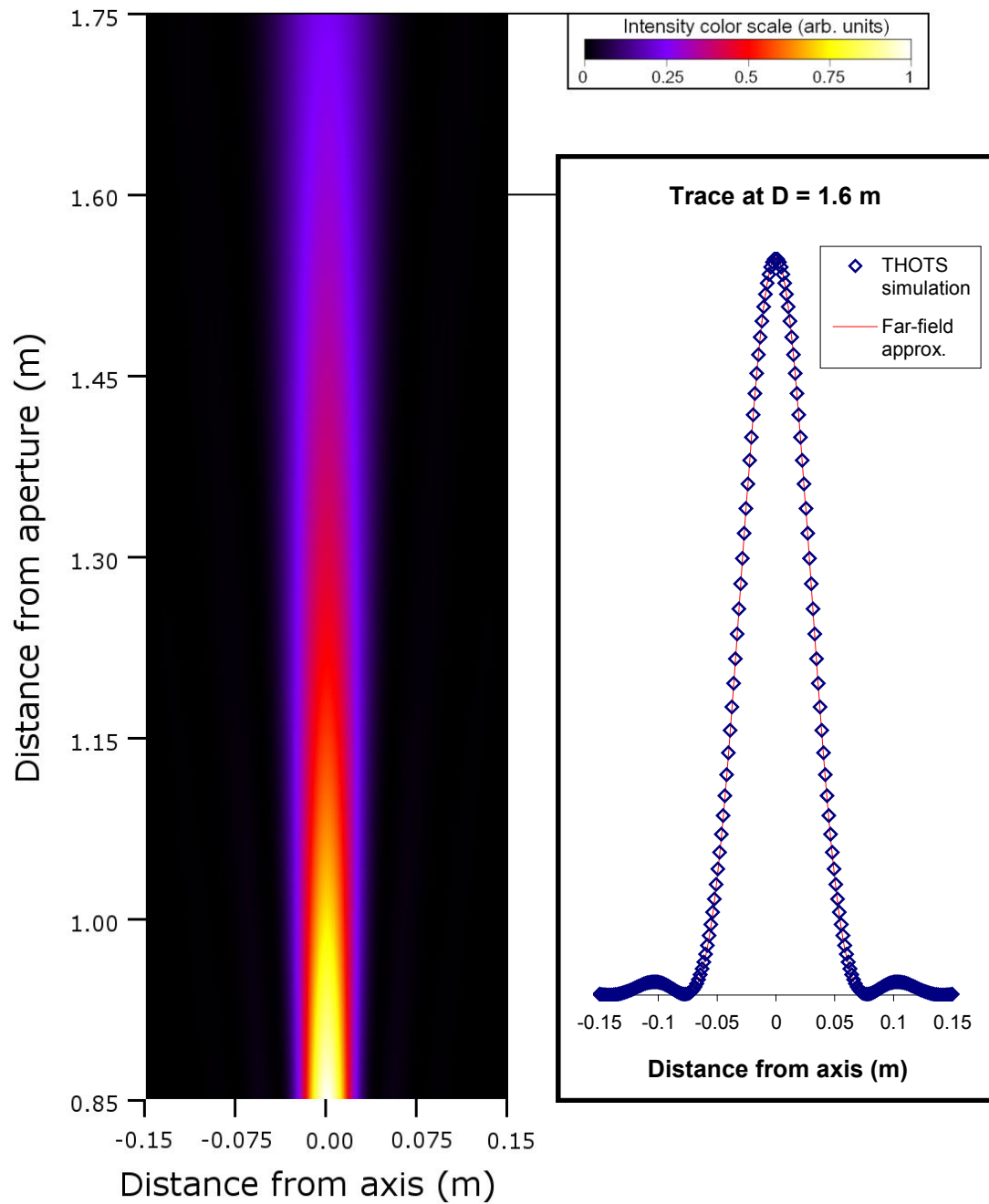


Figure 6. Far-field diffraction of a circular aperture. For this trace $\lambda = 1$ mm and aperture radius = 12.7 mm. *Left:* Cross-section of irradiance extending longitudinally from aperture. *Inset right:* Comparison of simulated irradiance profile trace to far-field approximation at a distance of 1.6 m.

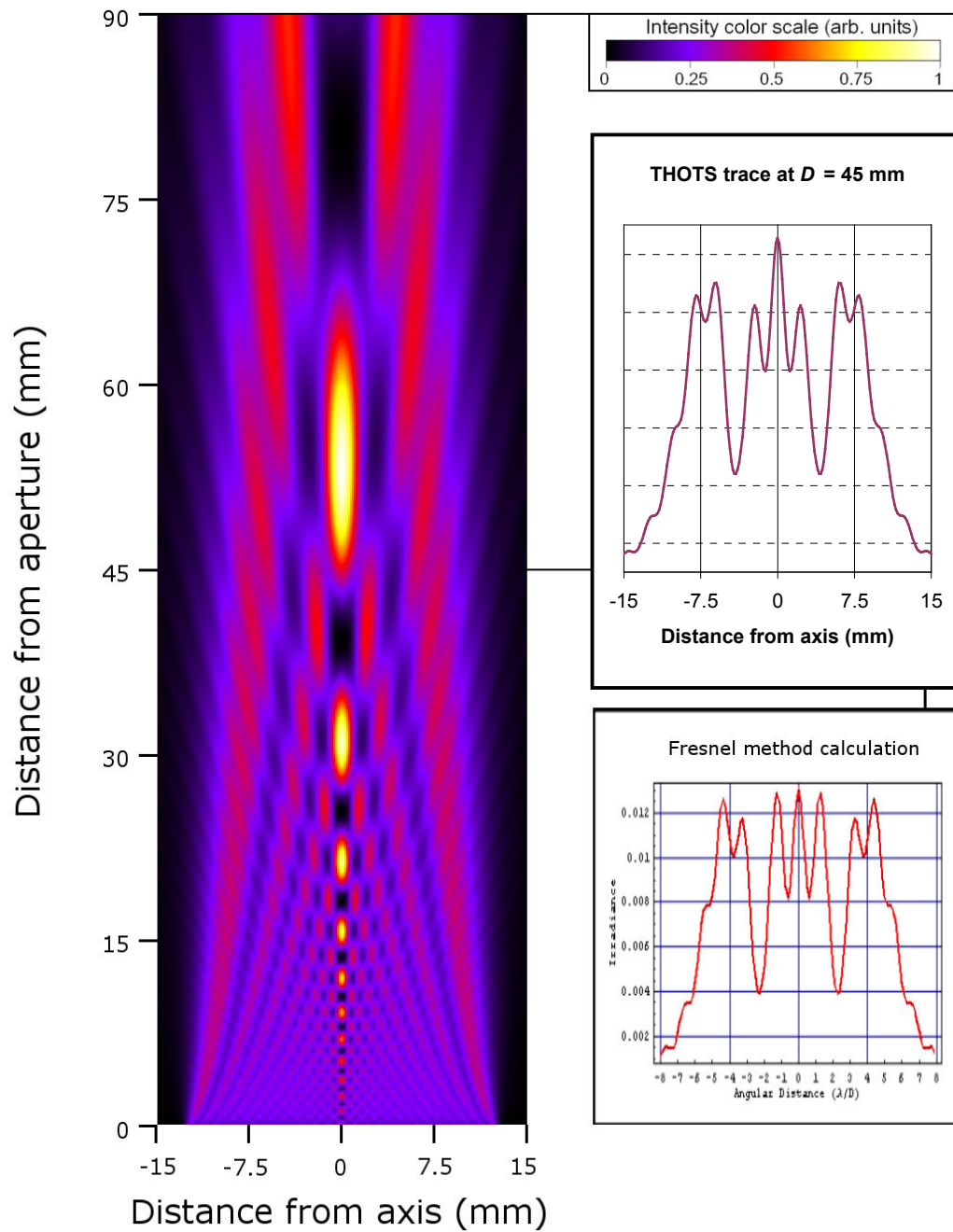


Figure 7. Extreme near-field diffraction of a circular aperture. For this trace $\lambda = 1$ mm and aperture radius = 12.7 mm. *Left:* Cross-section of irradiance extending longitudinally from aperture. *Center right:* Simulated irradiance profile trace at a distance of 45 mm. *Bottom right:* Irradiance profile based on near-field scalar Fresnel technique [15].

There are some small differences between the irradiance traces in Figure 7, notably off-axis. These may be due to the technique used by [15] where the Fresnel profile is based on a fast Fourier transform (FFT) method. The effective Fresnel zones at the aperture are calculated and the image is propagated forward by FFT with the inclusion of second-order phase factors to maintain accuracy in the near field. However, the two-dimensional transverse profile (not shown here) betrays less than perfect radial symmetry in that Fresnel-based calculation. Bilateral symmetry starts to creep in (breaking the expected radial symmetry) due to edge effects arising from the overall square shape of the source image. Furthermore, off-axis the pattern begins to distort somewhat, also due to the planar propagation.

These effects are common in FFT-based methods. Though it is also not shown here, the two-dimensional profile of the THOTS-generated irradiance at the $D = 45$ mm plane shows excellent radial symmetry. That this technique works well at distances so near the aperture without correction is remarkable in comparison. Of course the primary trade-off here is, again, more substantial processing time.

Another key thing to note is that while only near- and far-field examples are presented here, the mid-range distance should be solvable equally well. While most other techniques (such as the Fresnel method just mentioned) are specifically engineered to work in one range or the other, the inclusion of both $1 / kR$ and $1 / kR^2$ terms in (2.6) lets the code transition naturally from one region to the next.

As a demonstration of the three-dimensional application of this code, we next look at a parabolic mirror. In the laboratory, a standard off-axis parabolic mirror is

constructed as a cylindrical section of the surface of revolution of a parabola. For a 90° off-axis parabolic mirror there are two parameters. The first is the effective focal length (EFL) that is the distance from the cylindrical cut axis of the mirror to the off-axis location of the parabolic focusing point. The second is the diameter of the cylinder forming the parabolic section cut. It will be convenient to define the “cylindrical axis” as the axis of the cylindrical section as well as the “focal axis,” which is the line from the focal point to the 90° deflection point on the mirror. These axes necessarily intersect at this point and are perpendicular in the 90° off-axis case.

One principal use of this type of mirror is to collimate radiation onto the cylindrical axis for light emerging at some regular and divergent angle from the focal point. Alternatively, collimated light accepted along the cylindrical axis can be well focused along the focal axis and onto the focal point of the mirror. In our Michelson interferometer we expect to be transporting slightly divergent radiation. This is the reason for the initial collimating mirror shown in Figures 2 and 3. The light, then presumed to be traveling parallel to axis, is manipulated by the instrument before final focusing by secondary parabolic mirrors.

As the wavefront has some length to travel through the instrument before final focusing, we wish to investigate the behavior of a parabolic mirror in collimating mode. Shown in Figure 8 are the spectral fluence profiles through the center planes extending away from the mirror on the cylindrical axis of the mirror for $\lambda = 1 \text{ mm}$. The mirror is taken here to have an EFL of 6”, a diameter of 2” and an ideal vector point source placed at the focal point of the mirror radiating directly into the mirror.

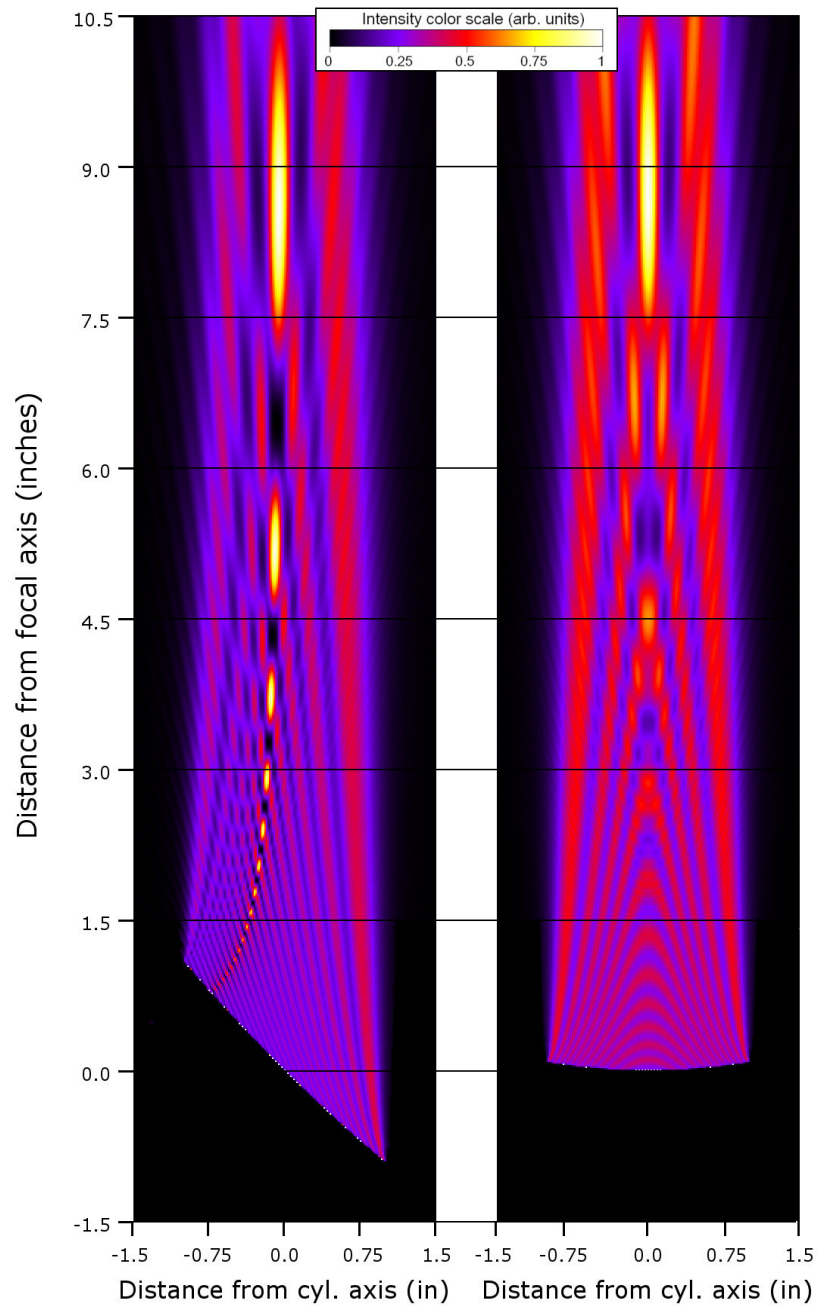


Figure 8. Diffraction by 6" EFL, 2" O.D. 90° off-axis parabolic mirror in collimating mode. Showing spectral energy distribution profile moving away from mirror along cylindrical axis. *Left:* Distribution in longitudinal plane containing focal axis and cylindrical axis. Point source to right at positive distance from cylindrical axis. *Right:* Distribution in plane containing cylindrical axis, normal to focal axis.

In Figure 8 we see the signs of diffraction limitation of the mirror. Compare this to Figure 7. In an absolutely ideal case where the wavelength of light is much smaller than the cylindrical diameter of the mirror, we expect the point source signal to be collimated into a circular wavefront. We indeed see that, as the wavelength becomes comparable to the cylindrical diameter of the mirror, the mirror acts as a circular diffraction aperture. Note the “peeling off” of secondary intensity peaks. These can escape detection by a mirror of the same diameter placed after the collimating mirror. It is worth noting that this signal modulation due to diffraction at the mirror is naturally wavelength dependent. Of course there is also some asymmetry observed due to the asymmetry of the mirror.

Limitations and Future Improvements

A number of challenges were encountered while attempting to implement this approach. The bulk of these stemmed from its numerical basis. While effort was made in finding analytic base equations that incorporate as much of the physics as possible in a very general way, the crucial Equations (2.6) require two-dimensional integration. Not sampling enough points leads to the creeping in of numerical error.

As the grid becomes more spread, out the approximately continuous surface begins to look like a set of separate radiating points. In effect the grid itself begins to look like a diffraction grating. Given the simple planar shape of the individual mesh elements, an attempt was made to counter this effect. We instead tried treating each

point in our mesh as filling its small element with constant illumination. This suggests a sort of aliasing technique, as is often used in image analysis. By modulating each point contribution with a simple sinc-function, the light from the point appears to be roughly that of an aperture.

This sampling method worked quite nicely, but only within the limits of near-perpendicular illumination and along directions parallel to the normal of the aperture. That limitation absolutely restricts the intention of the simulations that will involve 90° deflections for a wide range of incidences. For the time being this enhancement has been abandoned, but with improved expressions for “numerical aperture” diffraction effects, the THOTS code may stand to gain a significant performance boost.

Better integration techniques were attempted as well. Immediately it was recognized that most require additional points for interpolative fits of the surface curvature. Going to a Simpson integration technique, for example, effectively doubles the numerical aperture effect noted above. The primary points of interest become spread twice as far apart. So in this case an improvement over Euler integration was also temporarily abandoned.

The issue of the numerical aperture effect is notably wavelength dependent. As resolution is dropped or the wavelength shortens, secondary ghost images start sliding in. This is sensible as for a shorter wavelength the numerical aperture appears larger, thus enhancing the numerical diffraction effect. In the case where the mesh spacing is small compared to a wavelength, there is no noticeable effect. The size of

the equipment being modeled and the limit to the number of data points that can be calculated dictate the size of the mesh elements. It happens that for the size of the interferometer's optics that the code works very nicely in a wavelength range as low as $\sim 250 \mu\text{m}$. In the following chapters the study is carefully limited by this range.

The title of the software was in fact chosen due to its ability to operate in just the right range to analyze this problem. It can be extended somewhat with a slight strain on computation time. I note that the limit is not terribly concerning as it is expected that diffraction limitations for much shorter wavelengths would be minimal as compared to the mm range for optical elements with sizes in the hundreds of millimeters.

To maintain full generality, and as most of the above problems are solved with higher resolution, the obvious potential enhancement for THOTS is parallelization. With clusters becoming increasingly accessible at the academic level and multi-processor computers being available commercially, this seems a practical approach. Every increase in speed allows the code to probe deeper in the frequency range or to more quickly fill in a complete spectral scan of a problem.

The limits of the code were not appreciable enough to deter the following analyses. Though some considerable effort might be applied to quantify the error in more complex situations, tests of convergence at every stage have shown good agreement with other techniques.

CHAPTER IV

SINGLE-ELECTRON TRANSITION RADIATION MODELING

Transition Radiation Model Comparison

With the tools now developed, we turn to trends related to the problem at hand. Before modeling any coherent effects it is worthwhile to analyze single-electron radiation and perform some comparison to analytical models.

We begin with a schematic look at the resulting backward transition radiation at oblique incidence on a circular foil using the approach described in Chapter 3 as computed by the THOTS code. Figure 9 (left) shows the result for a $\gamma = 500$ electron as it collides with a 2" diameter foil at 45° incidence. A longitudinal profile of the $\lambda = 0.5$ mm wave propagating away from the foil is shown in the plane containing the incident beam and the normal to the foil. Here the electron travels in from the bottom of the page colliding with the foil at the vertex of the light curves. In this image, the intensity is plotted only up to the first 10% of the maximum value to highlight detail. The white regions are greater than this value. Also shown in Figure 9 is a trace at the center ($D = 19$ mm) of the image.

Aside from the lateral distortion, the resulting transverse wave (not shown) is otherwise a rotation of the trace shown in Figure 9. Note that now instead of a single bright cone there are several secondary peaks emerging in curved maxima. This is a

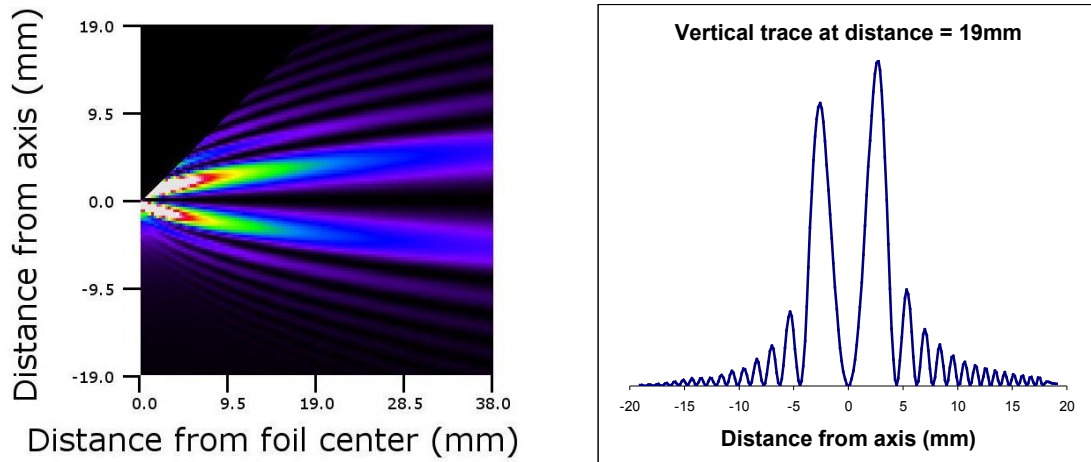


Figure 9. Spectral intensity distribution from backward single-electron radiation with circular foil at 45-degree incline. Values are $\gamma = 500$, $\lambda = 0.5$ mm, foil diameter $2''$. *Left:* Longitudinal cross-section of radiation for electron incident from bottom to top of image along left edge of frame. *Right:* Trace through center of image (left) at distance $D = 19$ mm.

near-field effect as we are close enough to see the contributions of all of the “radiators” of the foil, in agreement with [4]. The oblique angle gives rise to a rotational asymmetry of the TR, as has been noted in [3, 4, 5]. The primary intensity is seen to be concentrated in the two center lobes. In our case the inclusion of the z_0 phase factor in Equations (2.4) and (2.5) incorporates the “inclination factor” of [3, 4, 5]. These general features are present for other values of γ and λ , though it is worth mentioning that the radius of the primary maxima does vary [4].

At this point we see strong disagreement with the basic Ginzburg-Frank Equation (1.1). In comparison to the Liénard-Wiechert fields of a relativistic particle [10], the Ginzburg-Frank formula is found only to satisfy the “acceleration field” term. That is to say that the $1/R$ term of the Liénard-Wiechert field dominates. In comparison to the optical approach this is a statement that the far-field $1/kR$ term of

the transport integrals in Equation (2.6) dictate the diffraction pattern. However, as shown in [16], an analysis of the Liénard-Wiechert form shows that the “velocity field” ($1/R^2$) contribution starts becoming significant in the range $R > \lambda \gamma^2$. This becomes an imposing condition for even a medium-energy electron beam of ~ 15 MeV. In such a case the analysis of far-field dominated radiation in the mm range demands that we set up instrumentation at a distance of approximately one meter away before the far-field onset. (One should note that for ultra-relativistic beams this argument becomes quickly exaggerated.) It’s obviously impractical in practice to delay the measurement of the radiation over such long distances. At the very least the TR must clear a viewing window in the beam pipe before it can be propagated through any measurement instrument.

Fortunately we can build a theoretical construct that easily meets any selected length scale. A comparison to Equation (1.1) satisfying $R > \lambda \gamma^2$ is shown in Figure 10 for two different values of γ as a function of the axial distance ρ for backward TR generated at normal incidence. Parameters used were $\lambda = 1$ mm, distance from foil $R = 250$ m (to satisfy the far-field condition for $\gamma = 500$), and a foil diameter of 50.8mm. The Ginzburg-Frank formula predicts a dependence of the spectral fluence on γ^2 and a bright ring apex location that goes as $1/\gamma$. Therefore the axes have been scaled by the inverse of these factors for comparison. As a result of this scaling the prediction of the Ginzburg-Frank formula results overlap on the plot shown.

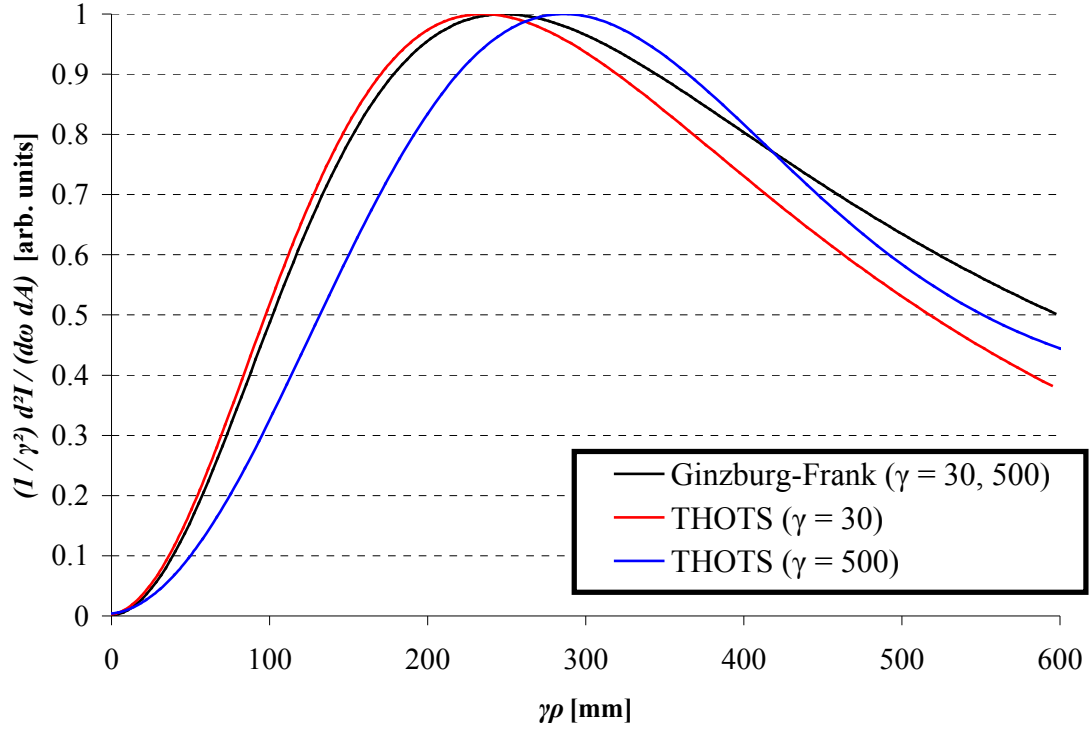


Figure 10. Spectral fluence traces along plane parallel to foil for far-field backward TR at normal incidence. Comparison of THOTS to Ginzburg-Frank Equation (1.1) with $\lambda = 1$ mm, foil diameter = 50.8 mm, and distance from foil $R = 250$ m. Here ρ is the perpendicular distance from the central axis.

Figure 10 shows very good agreement for $\gamma = 30$ near axis. At $\gamma = 500$ there is considerable difference. But again, for this beam energy a 250-meter observation distance is just at the onset of the far field, so some velocity (near) field effects may still be affecting the THOTS model.

For a near-field comparison I appeal to an analytic approximation derived by Bosch and Chubar to include the velocity field contribution in the paraxial limit [16]:

$$E_{\text{Transverse}} = \frac{e}{\pi \epsilon_0 c R} \cdot \frac{\sin(\pi R \theta^2 / 2\lambda)}{\theta^2} \quad (4.1)$$

Hereafter I will refer to Equation (4.1) as the Bosch-Chubar approximation.

Note that the Bosch-Chubar approximation is independent of γ and the radius of the aperture. By extended comparisons to the numerical THOTS approach, this has shown to hold well within the diffraction limitations of the aperture (foil) itself. That is to say that the radius of the foil must be several multiples of the wavelength ($\lambda \ll r_{foil}$).

The resulting spectral fluence profiles through the center plane for the component of the radiation propagating away from the foil are shown in Figure 11. Here a foil diameter of 50.8 mm was used with $\lambda = 1$ mm. For contrast, these images are plotted only to 10% of the maximum intensity. Transverse distributions (not shown) again exhibit complete rotational symmetry of the profiles shown.

For a clearer comparison, traces of the data in Figure 11 were taken at a distance from the foil of 25 mm. The resulting traces are shown in Figure 12 where these are again shown as a function of the perpendicular distance from axis ρ .

Figures 11 and 12 generally agree well with the analytic solution presented in [16] insofar as the locations of apex values near axis are concerned. The THOTS simulations agree with maxima not changing position with γ for $\lambda = 1$ mm. In the next section we will see that this is true over small ranges of γ when $\gamma > \sim 24$.

However, the chart in Figure 12 has all values normalized to that determined by the Bosch-Chubar Equation (4.1). At a fixed distance and λ , THOTS calculations dictate that a change in γ causes a change in the peak intensity. As of this writing it appears that numerically integrating the singularity at the origin of Equations (2.4) and (2.5) is affecting the peak value in the TR generation calculations, but not the form of

the distribution. We are seeking to resolve this issue for future studies where we plan to include absolute power measurements. This discovery effectively limits the final study of CTR interferometry in this paper to accounting only for diffraction effects and not TR generation frequency dependence.

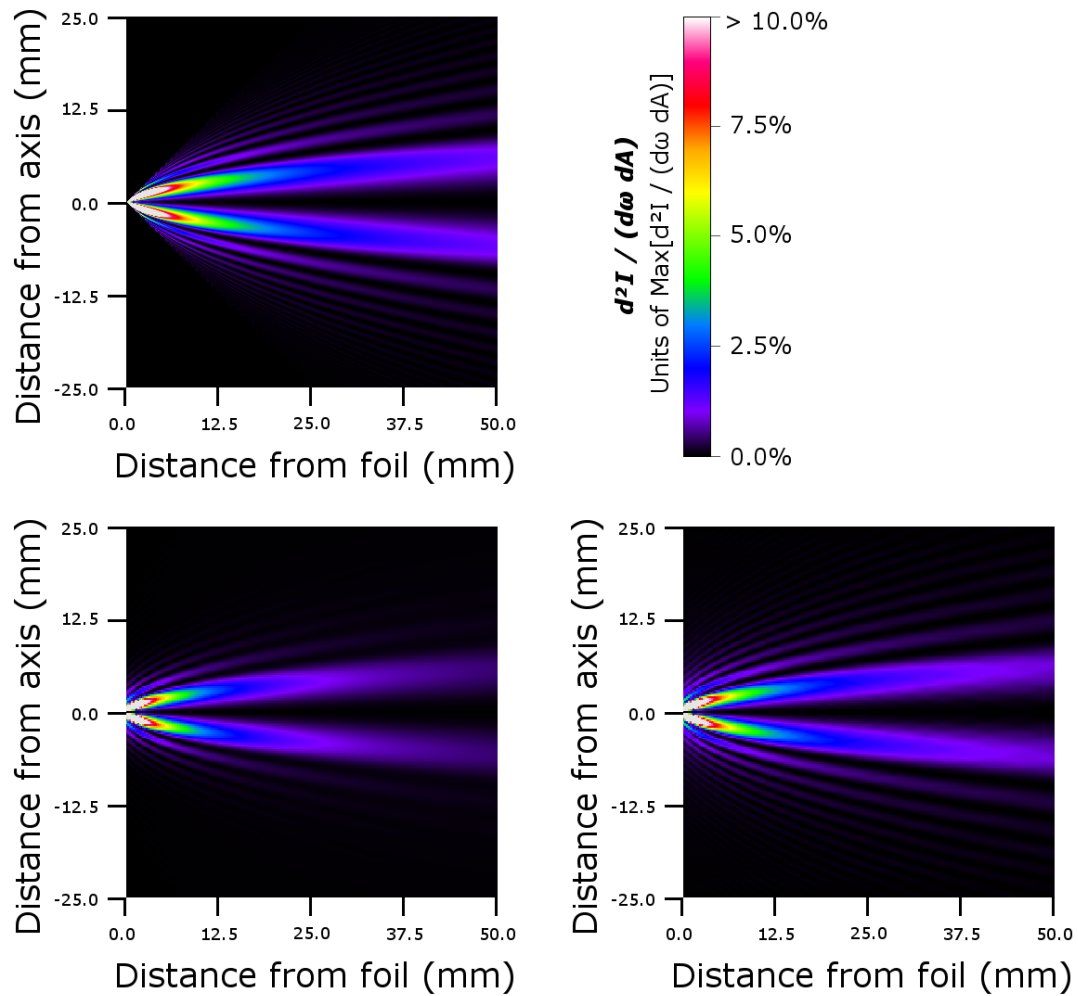


Figure 11. Spectral fluence profiles along center plane for near-field backward TR at normal incidence. Comparison of THOTS to Bosch-Chubar Equation (4.1) with $\lambda = 1$ mm, foil diameter = 50.8 mm. *Top Left:* Bosch-Chubar approximation, γ -independent. *Bottom Left:* THOTS prediction, $\gamma = 30$. *Bottom Right:* THOTS prediction, $\gamma = 500$.

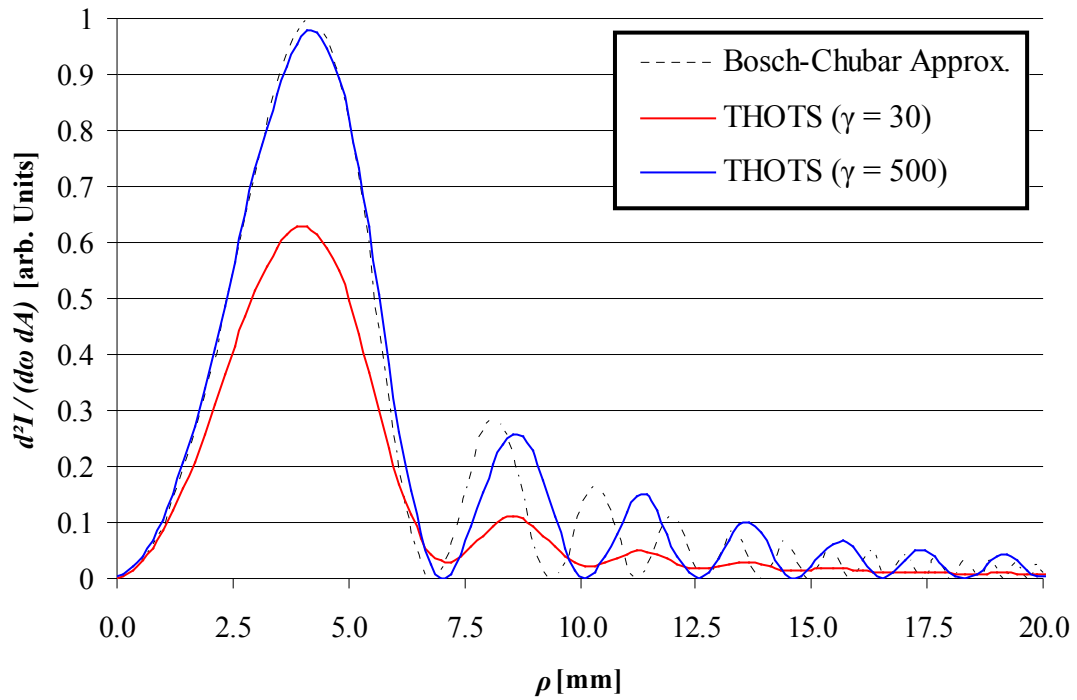


Figure 12. Spectral fluence traces along plane parallel to foil for near-field backward TR at normal incidence. Comparison of THOTS to Bosch-Chubar Equation (4.1) with $\lambda = 1$ mm, foil diameter = 50.8 mm, and distance from foil $R = 25$ mm. Here ρ is the perpendicular distance from the central axis.

The parameters chosen for Figures 11 and 12 were to reflect those of the subject interferometer which has $\gamma = 30$, foil diameter of 2" and bunch lengths that dictate the onset of significant CTR effects around 1mm. But for a still better comparison to the Bosch-Chubar equation, one should consider a larger foil, as Equation 4.1 assumes $r_{foil} \gg \lambda$, which is only marginally true for $r_{foil} \cong 25\lambda$. The impact of the foil radius is also analyzed more closely in the next section.

In general, a comparison to other models is somewhat challenging and difficult to disentangle as the THOTS model attempts to account for a variety of effects at

once. But with these generally fair results we now consider some trends as they may apply to the diffraction limitation problem.

Transition Radiation Apex Trends

With the first bright ring carrying the majority of the energy, anything that can affect its radius may alter integrated intensity measurements as the radius approaches the size of the various optical apertures. In this section we analyze how various parameters impact the position of the apex of the spectral intensity. The overall scale and distribution of energy among the primary and secondary rings will also affect the measured signal. Analyzing these more detailed trends in a general and quantitative way is difficult in principle when working with a numerical method. Fortunately specific configurations, such as that dictated by the Fermilab/NICADD photoinjector laboratory's interferometer, can be characterized readily as is done in the last chapter.

For the following few analyses single-electron radiation at normal incidence was analyzed at a distance from the foil equal to the distance of the quartz acceptance window (~ 8.2 cm) of the Fermilab/NICADD photoinjector. At each value of the independent parameters the spectral energy density was scanned for the maximum and the radius of the maximum was recorded. The values $\gamma = 30$, foil radius 25.4 mm and $\lambda = 1$ mm were used wherever possible because they apply to the Fermilab/NICADD photoinjector laboratory's experimental setup. The wavelength 1 mm was chosen

primarily because the THOTS code handles it quite easily while still being in the region of the coherent effect onset ($\lambda >$ bunch length $\approx 300 \mu\text{m}$).

Figures 13 and 14 show the dependence of the apex location on γ and r_{foil} respectively. This was done by scanning for the first maximum of the spectral fluence of the backward TR at perpendicular incidence for a distance corresponding to the distance between the center of the foil and quartz viewing window. The purpose here is to analyze the diffraction limitations for our setup at the acceptance aperture of the interferometer. The viewing window radius of 12.7 mm is also shown.

Figure 13 shows rather weak γ dependence for relativistic values. Scans for the parameters shown tend to remain weakly varying in tests out to $\gamma = 500$. As noted earlier, for a fixed λ , no appreciable effect on the spacing of the rings in more detailed images was ever noticed over changes in γ as large as ± 50 . Figure 13 shows this tendency to hold strongest down to a relatively modest $\gamma > \sim 24$. This dependence over significantly different energies is, however, wavelength dependent as will be seen in Figure 15. Again, this says nothing as to the scaling of the rings or the distribution of energy between them, which is yet to be determined.

Estimating the first TR spectral energy minimum as $\sim 2r_{apex}$, we see that the first ring will extend beyond the 1" diameter quartz window for long wavelengths (low frequencies). This information is critical in determining the structure of a bunch as one considers analysis of the inverse Fourier transform. Thus we see demonstrated here strong diffraction limitations of the divergent near-field TR.

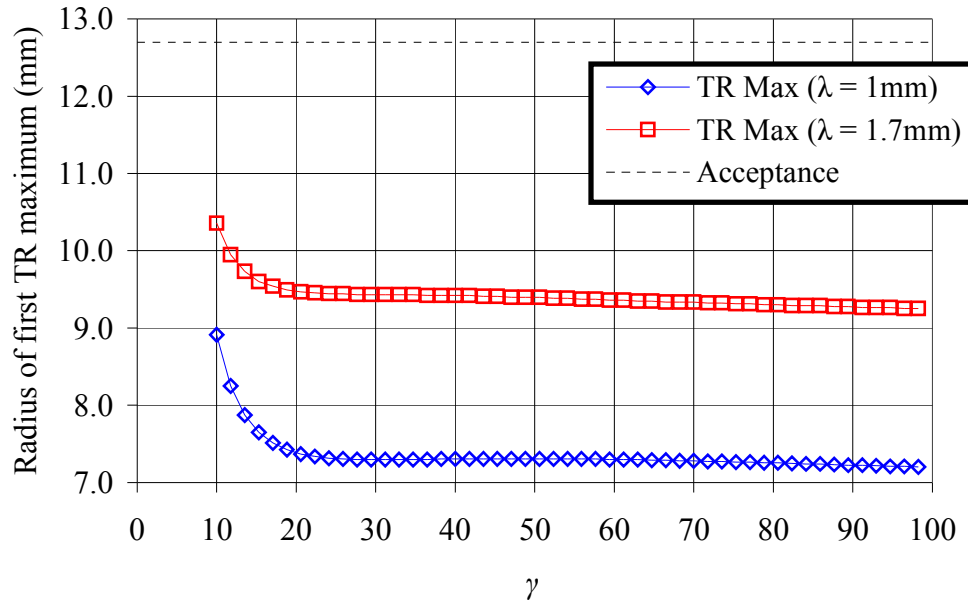


Figure 13. TR apex location as a function of γ . Distance from foil = ~ 8.2 cm, $r_{\text{foil}} = 25.4$ mm.

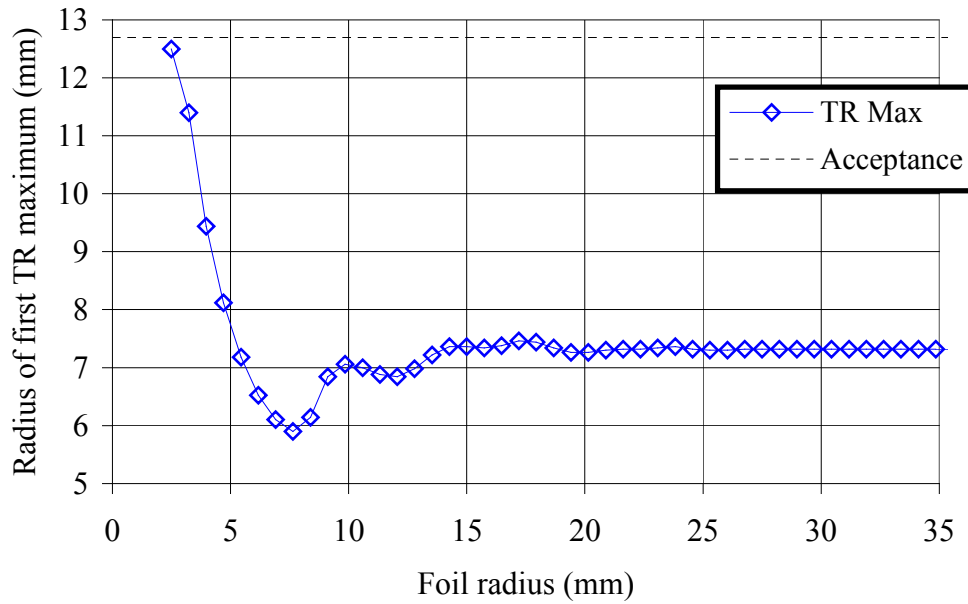


Figure 14. TR apex location as a function of r_{foil} . $\lambda = 1$ mm, distance from foil = ~ 8.2 cm, $\gamma = 30$.

Figure 14 demonstrates the foil behaving as a diffraction-limiting element itself. As r_{foil} and λ become comparable, analysis of spectral intensity profiles shows emission of r_{foil} / λ TR rings until $r_{foil} = \lambda$, at which point the simulation breaks down. In this final breakdown limit only one bright cone with a roughly 45° opening angle is seen in the near-field analysis. Of course where $r_{foil} \gg \lambda$ the foil begins to appear “infinite” and the signal modulation due to the finite foil becomes negligible. This indicates that the foil introduces an additional strong dependence of the emitted TR spectral intensity distribution on λ for low frequencies. Energetic suppression due to the foil size is likewise noted in [4].

Figure 15 shows the radius of the first bright ring as would be found at the viewing window for a 50mm diameter foil and the applicable $\gamma = 30$ while varying λ . Also shown is the prediction of the apex radius as determined by the paraxial Bosch-Chubar approximation of Equation (4.1). This is found to be $r_{apex} = \sqrt{R\lambda}$ where R is the distance from the electron-foil collision [16].

Though admittedly not conclusive until spectral energies are calculated, Figure 15 presents evidence of strong wavelength dependence on the acceptance of radiation into the instrument being used. We see that for the somewhat medium-energy beam under consideration there is a steadily increasing apex radius. However the problem becomes more pronounced for more relativistic γ where the wavelength dependence also introduces a more pronounced oscillatory behavior due to the longer formation length of the TR. This effectively lengthens the more oscillatory near-field region.

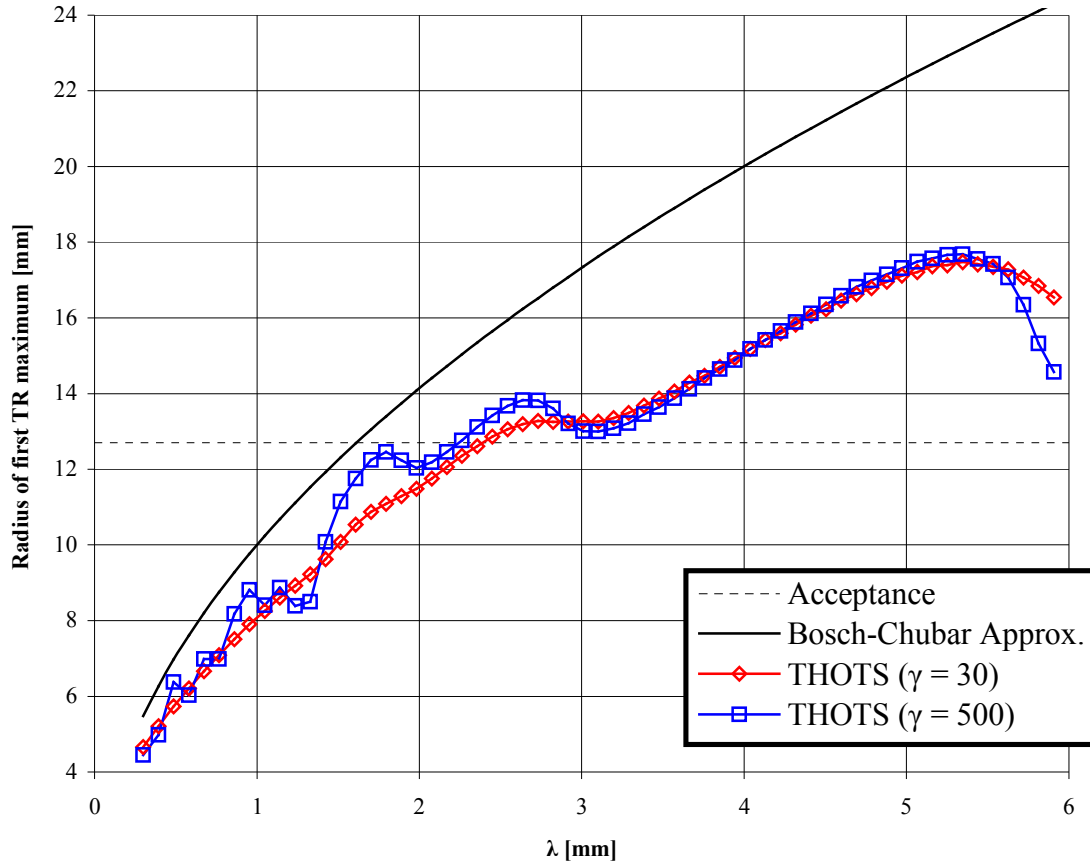


Figure 15. TR apex location as a function of λ . $r_{foil} = 25$ mm, distance from foil = ~ 8.2 cm. Comparison to Bosch-Chubar Equation (4.1).

At this point the evidence presented by the simulations suggests strong suppression of the low-frequency components of the spectral intensity. Again, if we estimate the first minimum as $\sim 2r_{apex}$, Figure 15 indicates that as $\lambda > \sim 0.5$ mm ($f < \sim 0.6$ THz) we begin to see clipping of the first bright ring at the acceptance window. For bunch lengths of ~ 300 μm it will be seen that these diffraction limitations can make reconstruction of a very simple bunch profile quite challenging when instrument diffraction response is not properly accounted for.

CHAPTER V

INTERFEROMETRY AND CTR MODELING

In this chapter I develop a simplified analysis of the Fermilab/NICADD photoinjector lab's Michelson interferometer. The emphasis here is particularly focused on demonstrating application of the THOTS code to finding the appropriate frequency responses of the instrument. To do so requires full wave propagation analysis of the instrument to get fully integrated spectral energies and is therefore very computationally demanding.

A proof of principle is straightforward enough using a simplified analysis of the instrument. Referring to the layout shown in Figures 2 and 3 I will assume that the collimation of the radiation at the first parabolic mirror is sufficient enough that the wavefront will be "clipped" along the edges only minimally before eventually arriving at the focusing mirror. Under this construction we can discard the intermediate mirrors and beam splitters. The optical path of the radiation is then "unfolded" to preserve the relative orientation of the remaining elements in the instrument. By conclusions drawn throughout this paper I suggest that the main contributions to signal attenuation in the instrument stem primarily from the clipping at the quartz acceptance window and perhaps at the focusing mirror and detector.

All that will be left of our idealized system is a 2" OD foil, 1" OD acceptance window, 6" EFL 90° off-axis collimating parabolic mirror of 3" OD circular section, 2" EFL 90° off-axis collimating parabolic mirror of 3" OD circular section, and a detector at the final focal plane of the system that has a 1/4" diameter acceptance aperture. The optical path length between elements and their relative orientations for the simulations are all taken from the instrument. We of course take the autocorrelation window as the optical path of interest.

Figure 16 shows a cartoon demonstration of a resulting simulation. Note that for illustration purposes the elements have been somewhat arbitrarily oriented such that the optical path is always in the same plane. This does not preserve the 3D optical path generated by a careful “unfolding” of the true optical path in the instrument, though path lengths are closely preserved in the drawing. That said, Figure 16 shows the irradiance profile component in the central plane containing the primary optical path along the primary direction of propagation. This schematic was generated using intensity and geometric outputs of the THOTS code for $\lambda = 1$ mm and $\gamma = 500$. Once again it is only plotted to a percentage of the maximum intensity to provide contrast.

The critical analyses of this section arise from investigation of the integrated values of intensity over transverse planes at the quartz acceptance window and final focal plane. Examples of the generated distributions are shown in Figure 17 for single-electron TR at three different wavelengths and $\gamma = 30$. On the left the spectral intensity distributions are given over planes of adaptive size at the plane of the quartz window. The green circles indicate the acceptance region of the viewing window.

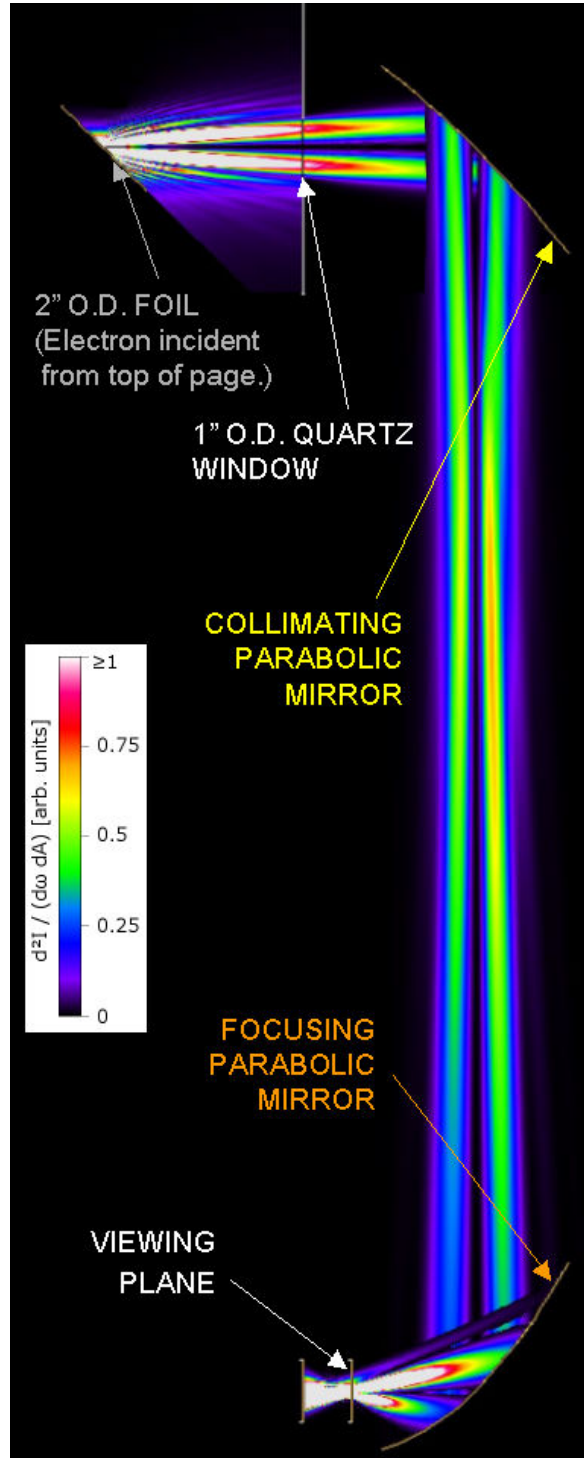


Figure 16. Schematic intensity profile of radiation propagating through an “unfolded” interferometer for single-electron TR. THOTS results for $\lambda = 1$ mm, $\gamma = 500$.

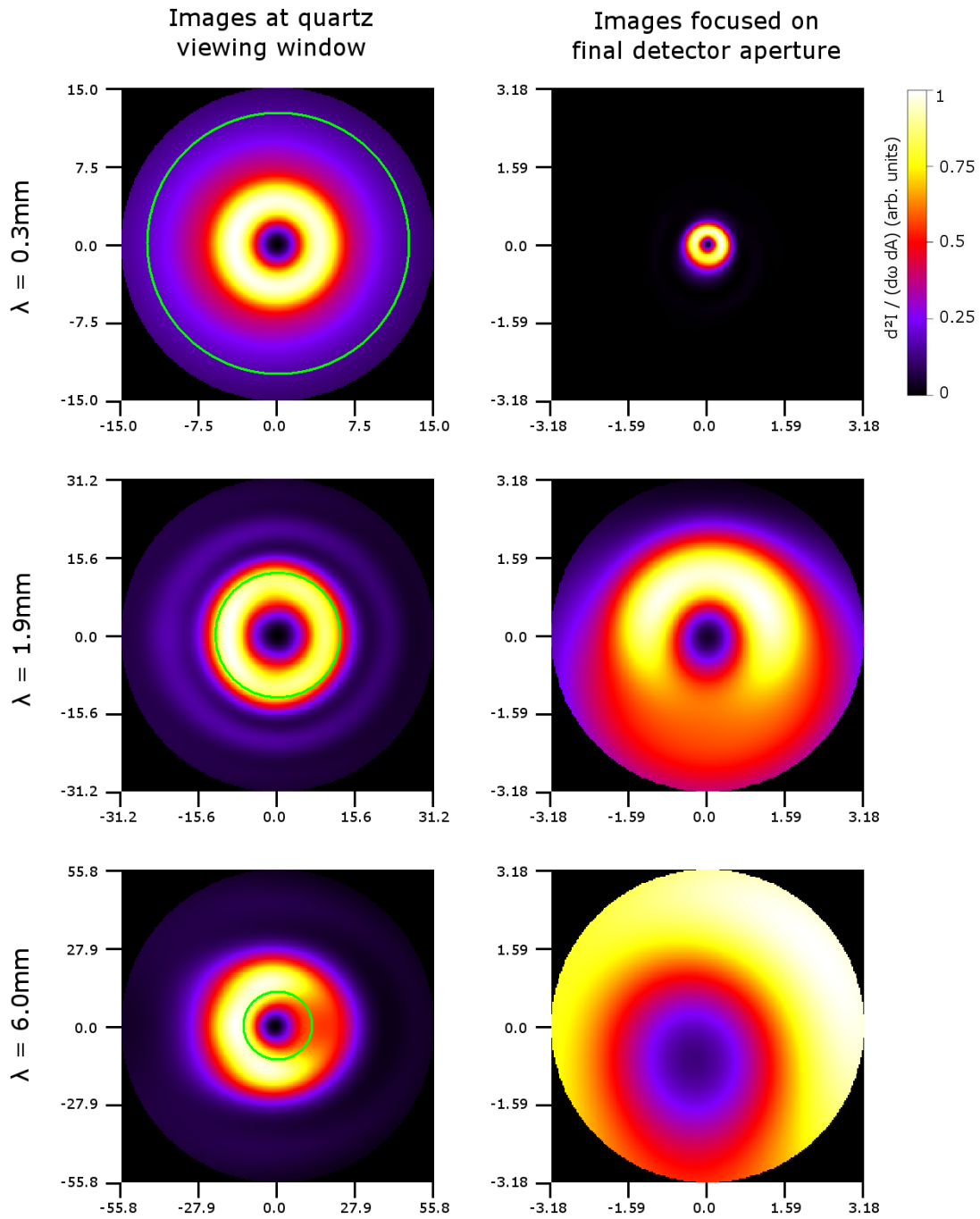


Figure 17. Intensity distribution images at instrument acceptance window and final detector for single-electron transition radiation for various λ . Green circles in images *left* indicate 1" diameter quartz window acceptance region. Geometric parameters taken from Fermilab/NICADD photoinjector interferometer and $\gamma = 30$. Axes indicate spatial coordinates in units of millimeters.

The right column of Figure 17 shows the final image arriving at the 1/4" diameter detector located at the focal point of the second parabolic mirror.

Asymmetry in both directions for these images is observed due to bilateral distortions introduced in different directions from the inclined foil and parabolic mirrors.

From these images we see more clearly the clipping of the TR wavefront. This is most pronounced at the quartz viewing window entrance to the instrument. However, for slightly larger wavelengths the instrument itself is found to have difficulty handling the very broad and easily diffracted wavefront leading to loss of signal at the small detector aperture.

I now set out to account for the several frequency dependencies observed throughout this paper. Our overriding goal is, of course, to weed out the mod-squared bunch form factor in Equation (1.7) as the inverse Fourier transform of the form factor yields the longitudinal bunch distribution. Three primary diffraction limitations, intrinsically frequency dependent, contribute to the terms in Equation (1.7). First, we consider that the electric field generated by the collision at the foil is essentially diffraction limited by the foil itself for large wavelengths and may be frequency dependent in the near field. These, as I will mention shortly, cannot be absolutely determined by the simulation at present. The second primary contribution arises from the limitation at the instrument's quartz viewing window. Finally, the instrument itself can add a further reduction of the signal before detection. Single-electron TR can also yield the impulse response of the system. Using this response information we will then proceed to correct a simulated CTR signal for a simple bunch.

The frequency dependence of the total integrated intensity $I_e(f)$ emitted by a single electron upon collision with the 2'' OD foil at 45° incidence and $\gamma = 30$ was calculated first. At this point I use the frequency expression $f = \omega / 2\pi$. As mentioned previously in reference to Figure 12, the numerical techniques presently used introduce an artificial frequency dependence of the peak intensity of calculated signals. This was attributed to the attempt to integrate the singularity in Equations (2.4) and (2.5) at the origin. While the peak intensity was altered, the change to the normalized distributions was never appreciable. We therefore assume that the resultant fields calculated are predicted accurately to within an overall scale factor.

Because of this, all subsequent integrated values are normalized to the initial simulated intensity $I_e(f)$. This effectively limits the following analysis to diffraction effects after the TR generation at the foil. This unfortunately means not accounting for observed diffraction limitations due to the finite foil for low frequencies, as they cannot be disentangled from the numerical effects that tend to cause a weak signal loss for higher frequencies.

While we cannot demonstrate quantitatively the low-frequency signal loss at the foil, we proceed with the analysis after TR generation. To see the effect of the instrument diffraction limitations we check the resulting response ratios for the quartz aperture as well as the instrument as a whole. These are given by the expressions:

$$R_{Aperture}(f) = \frac{I_{Aperture}(f)}{I_e(f)} \quad (5.1)$$

$$R_{Instrument}(f) = \frac{I_{Detector}(f)}{I_e(f)} \quad (5.2)$$

In Equation (5.1) $I_{Aperture}(f)$ refers to the THOTS-predicted integrated intensity over the instrument's quartz acceptance aperture. This corresponds to the regions in the green circles on the images of Figure 17 (left). Likewise, $I_{Detector}(f)$ refers to the integrated intensity over the final detecting aperture corresponding to the images of Figure 17 (right). The resulting ratios are shown in Figure 18.

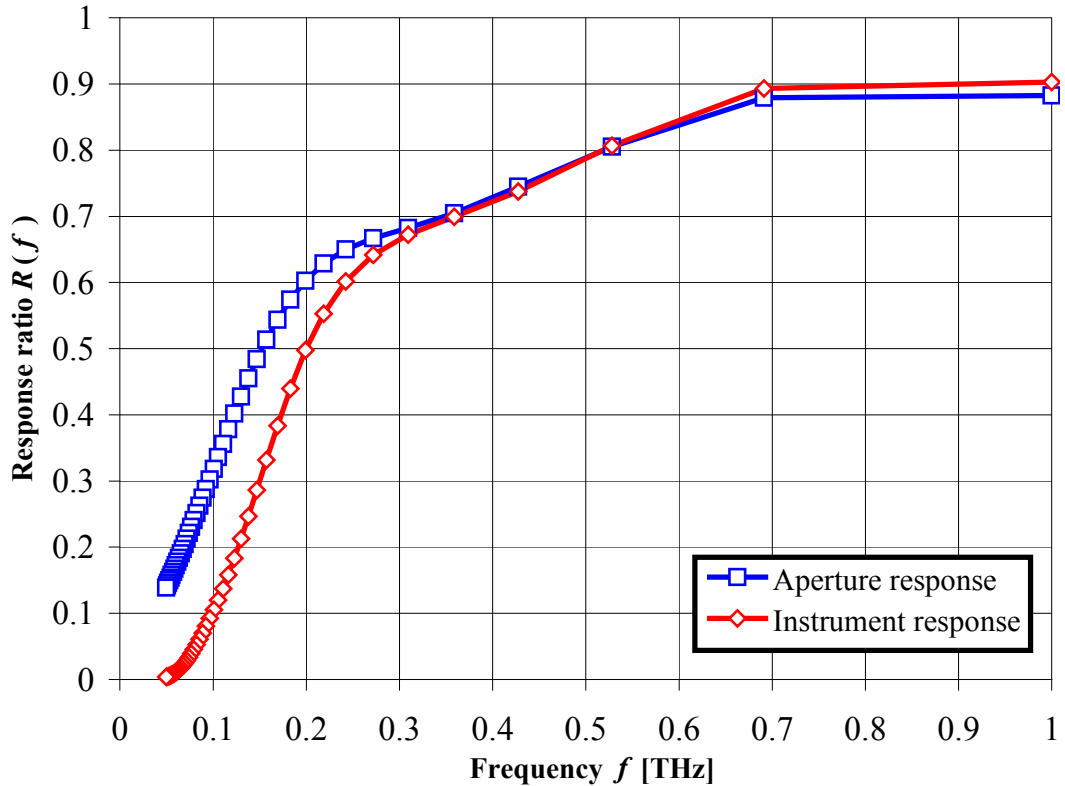


Figure 18. Response functions of acceptance aperture and instrument. Expressions for plots given by Equations (5.1) and (5.2). Geometric parameters taken from Fermilab/NICADD photoinjector interferometer and $\gamma = 30$.

The higher frequency values give the impression that the instrument actually enhances the signal before reaching the detector at higher frequencies. This is of course a numerical artifact as the combination of multiple sub-mm transport integrations are made worse by the low-wavelength, extreme near-field integration after the final focusing mirror. These tend to exaggerate the error of the code.

Figure 18 also shows a more detailed confirmation of the discussion regarding Figure 17. The primary contribution to the wavefront suppression stems from trimming at the quartz window with some additional signal suppression realized at lower frequencies.

The instrument response at its lowest investigated frequency of 0.05 THz shows the maximum accepted signal being reduced to about 0.4% its original value. Under experimental considerations this is discouraging if such a factor is sufficient to suppress the signal being measured to such a point that the signal-to-noise ratio becomes too great.

More importantly we consider the onset of the nonconstant response for frequencies less than 0.7 THz in the resolving of even the simplest bunches. This implies that if the bunch form factor (Fourier transform of the longitudinal bunch distribution) carries critical information for values less than 0.7 THz, any uncorrected CTR measurement can be grossly distorted.

Consider for example, as I will do shortly, a Gaussian longitudinal bunch distribution with a longitudinal $[FWHM]_z$ value of 300 μm . This is, of course, chosen to coincide with the theoretical bunch length at the Fermilab/NICADD photoinjector

lab. Still using the Fourier transforms normalized as in (2.2) we expect to have a form factor given as another Gaussian with root-mean-square frequency:

$$\sigma_f = \frac{c\sqrt{2\ln 2}}{\pi[FWHM]_z} \cong 0.375 \text{ THz} \quad (5.3)$$

For the CTR signal we therefore expect a signal modulated by a Gaussian squared form factor with Equation (5.3) providing the defining geometry. Assuming we knew to look for a Gaussian shape, note that we would be constrained primarily to its tail where the signal is sufficiently weak and tends toward incoherent. The region defining a pseudo-constant slope on the expected Gaussian would be in the 0.19 THz – 0.56 THz range. Attention to this part of the spectrum could yield a satisfactory analysis. But the nonconstant slope for the region below ~0.7 THz alters this information in an irregular manner. The obvious result is that if we had the signal spectrum and tried direct analysis of its inverse Fourier transform we would likely get an erroneous bunch profile.

Of course in practice there are experimental tricks for resolving a pseudo-system impulse response as well as trial-and-error numerical fitting techniques for fixing the data collected. However, assuming the physical model employed in THOTS to be a reasonable approximation and sufficiently numerically accurate, let us attempt to repair a THOTS-simulated CTR signal of the ideal Gaussian bunch discussed above using the response signals modeled in this chapter.

Construction of the signal resulting from a bunch of finite longitudinal extent follows quite closely to that employed in single-electron TR with one alteration: At the

start of the run we superimpose the contributions to the electromagnetic field of several electrons at different positions around the foil. For this analysis the bunch is taken to be a line charge distribution with no transverse dimensions. It is constructed such that we look at the radiation emitted the instant the center of the Gaussian bunch is passing through the foil. Numerically this was accomplished by taking 100 macro-particles spaced evenly over the range $\pm 2\sigma_z$ along the propagation axis each weighted by the value of the Gaussian with a $FWHM_z$ value of 300 μm . This is done such that the total charge of the line-bunch equals $1e$ so the N^2 term of Equation (1.7) is unity. This signal summed up as a source, the resulting CTR is propagated through the simulated instrument to our virtual detector in precisely the same manner as done in the previous TR response analysis of this chapter. To analyze the result we now recast Equation (1.7) to include the signal reduction due to the instrument:

$$I_{Detector,CTR}(\omega) \propto N^2 R_{Instrument}(\omega) I_e(\omega) |f(\omega)|^2 \quad (5.4)$$

Again, to be explicit, $f(\omega) = \int_{-\infty}^{\infty} \rho(z) \exp(-ikz) dz$, the form factor of the bunch. As our simulation corresponds to zero path (phase) difference and the form factor has only real components, we express the last factor in Equation (5.4) as:

$$|f(\omega)|^2 = f^2(\omega) \quad (5.5)$$

where $f(\omega)$ corresponds to a Gaussian with standard deviation derived in Equation (5.3) for our simplified simulated experiment. In an experimental sense, $f(\omega)$ is what we are always seeking to determine as it carries the information of the bunch profile. So rearranging (5.4) to dig out the form-factor-squared term:

$$f^2(\omega) \propto \frac{I_{Detector,CTR}(\omega)}{N^2 R_{Instrument}(\omega) I_e(\omega)} \quad (5.6)$$

The final comparison is presented in Figure 19. The red diamonds represent the simulated integrated spectral intensity at the detector aperture normalized by the simulated $I_e(\omega)$. The normalization is done to restrict interest to diffraction effects. For comparison, the theoretically calculated form factor squared (FFS) is plotted. Note the strong suppression of the signal from the ideal FFS form. Strong signal suppression is observed owing to the diffraction limitations of the equipment.

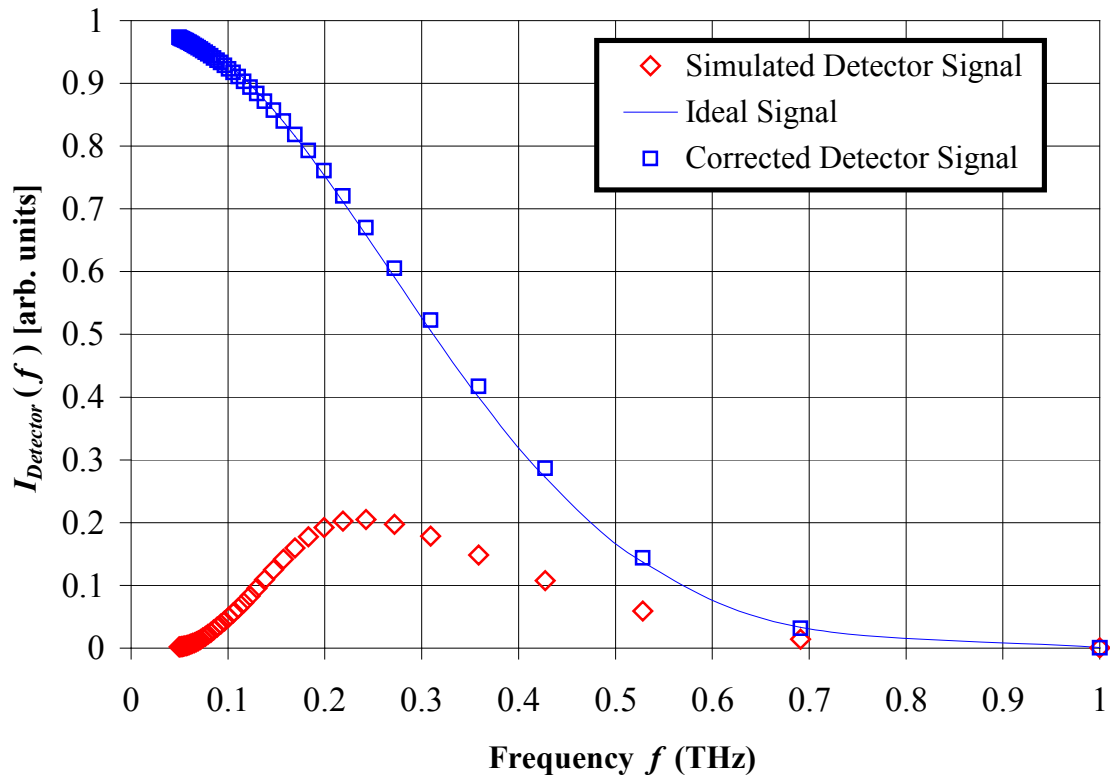


Figure 19. CTR signal due to 300 μm FWHM line charge distribution and subsequent correction using THOTS-calculated system frequency responses. Ideal signal is Gaussian-squared with $\sigma_f \approx 0.375$ THz. Expressions for corrected signal given by (5.6). Geometric parameters taken from Fermilab/NICADD photoinjector interferometer and $\gamma = 30$.

Again, as the FFS term relates to the longitudinal bunch profile, we wish to eliminate all other terms of Equation (1.7). Correcting the simulated detector signal using Equation (5.6) and the response shown in Figure 18 produces the plot of blue squares in Figure 19. A closer look shows a smooth comparison between the ideal and corrected simulation FFS within a $\pm 1.5\%$ error.

Comparison of the uncorrected CTR signal in Figure 19 to its ideal value implies a strong deviation from the expected value. Assuming the THOTS model of TR generation and propagation to be even approximately accurate, analysis of the inverse Fourier transform produced by inspection of this FFS will clearly not reproduce our simple Gaussian bunch. However, the corrected signal represents the ideal signal much more cleanly. Analysis of this repaired signal will likely produce much more accurate information with regards to the longitudinal distribution.

CHAPTER VI

FINAL REMARKS

Conclusions

Strong evidence was given at the end of the previous chapter as to the self-consistency of the THOTS simulations. While several canonical diffraction patterns were benchmarked in our full evaluation of the code, some question may still lurk as to the validity of the rigorous application of the virtual photons method outlined in Chapter 2. This is especially true of finding a numerical solution that sets an absolute scale for the resulting TR and CTR. However, the previous chapter also suggests that a full system response correction can be determined with these tools such that effects otherwise difficult to justify can be easily resolved. An experimental basis as to the accuracy of this method can be found by consideration of data our group already has in hand. This highly detailed correction could prove a useful enhancement for CTR-based diagnostics.

For the parameters dictated by the experiment analyzed it was also observed that we were stuck in a position where several effects battled to dominate the frequency response at different parts of our range of interest. These are all dictated by the multiple effect combinations given by scales of wavelength, beam energy, observation distance and optical aperture sizes. While these effects can be difficult to

unravel, the technique shown here appears to account for all effects simultaneously in a given system and with much weaker restrictions on the various parameters.

Future Plans

Many of the future developments being considered hinge on the optimization of the code. The present version of THOTS employs only the simplest of algorithms for evaluating the system described throughout the paper. It was an absolutely minimal implementation found to be just fast and accurate enough for the job while providing an excellent proof of principle. But any calculations requiring the scanning of more than one parameter or integrations over more than a few surfaces (including volume integration) lead to magnified numerical error and excessive processing times.

Sans optimizations, the code is still prepared for a detailed analysis of the interferometer frequency response in a manner that applies more directly to the experiment. I refer to the gross simplifications made in the idealized instrument presented with regard to the phase information of the modulus-squared form factor. In the experiment the phase information of the complex form factor is required for comparison to the path delay phase reconstruction relations expressed in Equations (1.8) – (1.11). By either clever manipulation of the phase information held in the fully complex solution of the THOTS calculations or an exact model of the experiment, one can recover the response as it pertains to the autocorrelation function $S(\delta)$. In the current version an exact model would, however, require a large though not

unreasonable amount of computing time as we would necessarily have to scan both the frequency and path differences.

Coherent diffraction radiation (CDR) may also be readily explored with the present code. The setup for a CDR experiment is essentially the same as that for CTR, but with a hole in the center of the foil. This is useful for avoiding foil destruction in highly energetic or high-current beams. Such a foil would be a simple construction in terms of the THOTS surface meshing ability with all other treatment remaining the same. So long as the foil is thin and flat, no further adaptation would be required. Exotically shaped apertures in the foil could also be considered.

Should great optimizations be added, volume integrations would also be possible. This could allow propagation of the radiation in regions where there are many secondary reflections, such as that for a divergent signal entering the large end of a hollow metallic cone. Such cones are frequently used as antennae for channeling large wavefronts down into small detector openings.

It is also worth mentioning that 3D surfaces more exotic than foils or cones could also then be modeled. This could have great utility in investigating new ways to manipulate CTR for large-bandwidth THz sources or for diagnostics applications.

The freedom to perform volume integrations may also allow for the analysis of nonlinear effects, another of my research interests. One ambitious example is found in optical rectification in nonlinear crystals. These so-called “electro-optic” (EO) crystals can be used to generate THz radiation when driven by fs-lasers. Such a calculation would be extremely demanding in the current version of the software. But

if made feasible by further code developments, a highly detailed picture of the THz radiation generated by the pumping of EO crystals could be realized.

REFERENCES

- [1] V. L. Ginzburg, "Transition Radiation and Transition Scattering", *Phys. Scr.* **T2A**, 182-191 (1982).
- [2] L. D. Landau and E. M. Lifschitz, *Electrodynamics of Continuous Media*, 2nd Edition, Pergamon Press, Oxford (1984).
- [3] J. van Tilborg, "Coherent Terahertz Radiation from Laser-Wakefield-Accelerated Electron Beams", Ph.D. Thesis, Eindhoven University of Technology (2006).
- [4] S. Casalbuoni, B. Schmidt and P. Schmüser, "Far-Infrared Transition and Diffraction Radiation", TESLA Report 2005-15.
- [5] C. Settakorn, "Generation and Use of Coherent Transition Radiation from Short Electron Bunches", Ph.D. Thesis, Stanford University (2001).
- [6] D. Mihalcea, C. L. Bohn, U. Happeck, and P. Piot, "Longitudinal Electron Bunch Diagnostics Using Coherent Transition Radiation", *Phys. Rev. Special Topics - Accelerators and Beams* **9**, 082801-1 - 082801-7 (2006).
- [7] C. A. Brau, *Modern Problems in Classical Electrodynamics*, Oxford University Press, Oxford (2004).
- [8] *Mathematica for Linux 5.2*, Stephen Wolfram, Wolfram Research (2005).
- [9] E. Hecht, *Optics*, 4th Edition, Addison Wesley, San Francisco (2002).
- [10] J. D. Jackson, *Classical Electrodynamics*, 3rd Edition, John Wiley and Sons, New York (1998).
- [11] C. T. Tai, "Direct Integration of Field Equations", *PIER* **28**, 339-359 (2000).
- [12] J. A. Stratton and L. J. Chu, "Diffraction Theory of Electromagnetic Waves", *Phys. Rev.* **56**, 99-107 (1939).

- [13] A. S. Marathat and J. F. McCalmont, “Vector Diffraction Theory for Electromagnetic Waves”, *J. Opt. Soc. Am. A.* **18**, 2585-2593 (2001).
- [14] W. H. Press, S. A. Teukolsky, W. T. Vetterling and B. P. Flannery, *Numerical Recipes in C*, 2nd Edition, Cambridge University Press, Cambridge (2002).
- [15] J. C. Wyant, “James C. Wyant – Fresnel Diffraction for Circular Aperture”, University of Arizona College of Optical Sciences, <http://wyant.opt-sci.arizona.edu/fresnelZones/fresnelZones.htm>.
- [16] R. A. Bosch and O. V. Chubar, “Long-Wavelength Edge Radiation in an Electron Storage Ring”, *Synchrotron Radiation instrumentation: Tenth US National Conference*, AIP Conference Proceedings **417**, 35-41 (1997).